Virtual image patch-based cloud removal for Landsat images

Zhanpeng Wang[a], Yinghai Ke[a,b,c*], Demin Zhou[a,b,c], Xiaojuan Li[a,b,c], Lin Zhu[a,b,c], Huili Gong[a,b,c]

[a] College of Resource Environment and Tourism, Capital Normal University, Beijing, 100048, China;

[b] Beijing Laboratory of Water Resources Security, Capital Normal University, Beijing, 100048, China

[c] Laboratory Cultivation Base of Environment Process and Digital Simulation, Capital Normal University, Beijing, 100048, China.

Corresponding Author: Yinghai Ke, Ph. D, yke@cnu.edu.cn

Virtual image patch-based cloud removal for Landsat images

Abstract

The inevitable thick cloud contamination in Landsat images has severely limited the usability and applications of these images. Developing cloud removal algorithms has been a hot research topic in recent years. Many previous algorithms used one or multiple cloud-free images in the same area acquired on other dates as reference image(s) to reconstruct missing pixel values. Although it has been widely recognized that reference image(s) has great impacts on the performances of cloud removal algorithms, it still remains challenging to determine the optimal reference image(s). In addition, abrupt land cover change can substantially degrade the reconstruction accuracies. To address these issues, we present a new cloud removal algorithm called Virtual Image patch-based Cloud Removal (VICR). For each cloud region, VICR reconstructs the missing surface reflectance by three steps: virtual image patch construction based on time-series reference images, similar pixel selection using the newly proposed temporally weighted spectral distance (TWSD), and residual image estimation. By establishing two buffer zones around the cloud region, VICR allows automatic selection of the optimal set of time-series reference images. The effectiveness of VICR was validated at four testing sites with different landscapes (i.e., urban, croplands and wetlands) and land change patterns (i.e., phenological change, abrupt change cause by flooding and tidal inundation), and the performances were compared with mNSPI (modified neighborhood similar pixel interpolator), WLR (weighted linear regression) and ARRC (AutoRegression to Remove Clouds). Experimental results showed that VICR outperformed the other algorithms and achieved lower

Root Mean Square Errors in surface reflectance estimation at the four sites. The improvement is particularly noticeable at the sites with abrupt land change. By considering the difference in the contributions from each reference image, TWSD improved the ability of VICR in predicting abrupt change in surface reflectance. Moreover, VICR is more robust to different cloud sizes and to changing reference images. VICR is also computationally faster than ARRC and mNSPI. The framework for time-series image cloud removal by VICR has great potential to be applied for large datasets processing.

Keywords: Cloud removal; Virtual image; TWSD; Time-series images; Landsat

1. Introduction

Remote sensing imagery acquired by optical satellite sensors are important earth observation data sources and play irreplaceable roles in the studies of global climate change and natural resources management (Kokhanovsky, 2013; Nijland et al., 2019; Wang et al., 2021b). Among the optical satellite sensors, the Landsat series, including Thematic Mapper (TM), Enhanced Thematic Mapper (ETM+), Operational Land Imager (OLI) are possibly one of the most widely used owing to their medium spatial resolution, regular revisit cycle and long-term data continuity (Zhu et al., 2020; Huang et al., 2021). However, cloud contaminations in Landsat images are inevitable because approximately one-third of global land area is obscured by clouds. For some areas, the probability of cloud cover is even higher (Shen et al., 2015; Cao et al., 2020). Clouds and their shadows lead to significant reductions in the availability of valid observations and restrict real-time monitoring of land surface change (Wang et al., 2021b; Li et al., 2021). Compared to thin clouds, thick clouds result in missing image values as they completely block the electromagnetic energy reflected from the land surface. Reconstruction of the images covered by thick clouds and their shadows (hereafter we call cloud removal) has become a hot research topic for the purpose of wider application of time-series Landsat images (Shen et al., 2015; Chen et al., 2017; Luo et al., 2018; Zhang et al., 2021).

The basic idea of cloud removal approaches is to predict unknown pixels in cloud/shadow areas with the assist of known information. According to the sources of auxiliary information, cloud removal methods can be divided into three categories: (1) single image-based methods, (2) multi-sensor image-based methods, and (3) single-sensor reference image(s)-based methods. Single image-based methods restore cloud pixels based on the assumption that the missing data and the surrounding cloudless data share the same statistical distribution or geometric structures. Typical methods include spatial interpolation (Siravenha et al., 2011; Li et al., 2014), and deep learning algorithms such as Generative Adversarial Networks (Xu et al., 2021; Zheng et al., 2021). These methods do not require additional data source, while produce unreliable results for large cloud (Cao et al., 2020; Zhang et al., 2021; Zheng et al., 2021). The second category of methods uses auxiliary information from different sensors such as synthetic aperture radar (SAR) images that are less affected by cloud, or MODIS images that have short revisit cycle (Li et al., 2019; Shen et al., 2019; Gao et al., 2021; Meraner et al., 2020). Due to radiometric inconsistencies and spatial resolution discrepancies, these methods have limited performances in areas with complex spatial patterns (Li et al., 2019; Shen et al., 2019; Meraner et al., 2020). Single-sensor reference image(s)-based methods utilize cloud-free images acquired by the same sensor on other date(s) as reference image(s). The spectral and spatial relationships between the neighboring pixels and the cloud pixels (also called target pixels) are quantified based on the reference image(s) and used to fill the missing values (Chen et al., 2011; Zhu et al., 2012; Zeng et al., 2013; Vuolo et al., 2017; Malek et al., 2018; Cao et al., 2020; Zhang et al., 2020; Zhang et al., 2021; Xu et al., 2022). As images acquired by the same sensor (e.g., Landsat TM/ETM+/OLI) are not affected by radiometric or geometric inconsistencies, this type of methods has become the mainstream for thick cloud removal. Representative and commonly used methods include Neighborhood Similar Pixel Interpolator (NSPI) (Chen et al., 2011), improved neighborhood similar pixel interpolator (mNSPI) (Zhu et al., 2012) and weighted linear regression model (WLR) (Zeng et al., 2013).

Most previous research relied on one cloudless image as the reference image (Zhu et al., 2012; Cheng et al., 2014; Zhang et al., 2018; Xu et al., 2022). The reconstruction accuracies depend on the similarity between the reference image and the cloud image. Generally, larger time interval between the reference image and the cloud image indicates weaker correlation between them (Lin et al., 2013; Du et al., 2019). Recent methods proposed utilization of multi-temporal reference images (Chen et al., 2017; Cao et al., 2020; Zhang et al., 2020). For example, Chen et al. (2017) sorted multi-temporal reference images and utilized the most similar three reference images. Cao et al. (2020) proposed AutoRegression to Remove Cloud (ARRC) algorithm which uses multi-year (normally 3-4 years) Landsat surface reflectance time series to restore missing data. Zhang et al. (2020) proposed a spatio-temporal patch group deep learning framework based on multi-temporal images. Incorporation of multiple reference images effectively reduce the dependency on a single reference image. However, it is still difficult to determine the optimal set of reference images because too much dependency on time series reference information might lead to adverse effect when abrupt land cover change occurred in the cloud image (Cao et al., 2020; Zhang et al., 2021).

Another key to the success of cloud removal algorithms is how to integrate the reference information to fill the missing values. Two types of strategies, i.e., pixel-based and patch-based strategies have been proposed. Pixel-based strategy aims to predict values of each target pixel based on neighboring pixels. Similarity metrics between neighboring pixels and the target pixel are usually developed to select similar neighboring pixels and to predict target pixel value (Zhu et al., 2012; Cheng et al., 2014; Chen et al., 2017 ;Cao et al., 2020). However, it is difficult to determine whether the similar pixels are still similar to the target pixel at the time of cloud image acquisition. Abrupt land cover change can lead to obvious change in the target cloud pixel, thus utilization of "similar" pixels during other time leads to reconstruction errors (Chen et al., 2018; Li et al., 2019). To alleviate the errors, reference images with greater similarities with the targe image should be paid greater attention in similar pixel selection. Patch-based strategy involves learning relationships between pairs of cloudless and the simulated cloud-contaminated image patches as training datasets. Deep learning models, such as spatio-temporal patch group deep learning framework have been developed (Zhang et al., 2020). However, to date the proposed deep learning models primarily aimed to restore textural and structure patterns in the target image rather than achieve high accuracy of the surface reflectance estimation of individual pixels (Zhang et al., 2020; Zhang et al., 2021; Xu et al., 2022). For example, Xu et al. (2022) reconstructed Landsat Level-1 digital number images and the 16-bit images were down sampled to 8-bit. In addition, requirements for large number of training datasets and the complex parameter settings of deep learning restrict its wide applications for operational cloud removal.

In this study, we propose a new cloud removal algorithm for Landsat surface reflectance (SR) images that we call Virtual Image patch-based Cloud Removal (VICR). It combines patch-based virtual image construction and pixel-based prediction by using temporal, spectral and spatial information in time-series reference images. The idea of virtual image is to produce a synthesis reference image patch based on time-series reference images, which is closer to the image at the prediction time than any of the original reference images. Although the concept of virtual image was developed for spatio-temporal fusion of Landsat and MODIS data (Wang et al., 2020), it is introduced in cloud removal for the first time. In addition, VICR provides two functions different from previous cloud removal algorithms: (1) it allows automatic selection of the optimal set of temporal reference images; (2) it provides a new similarity index, namely temporal weighted spectral distance (TWSD), for similar pixel selection that aims to reduce prediction errors caused by temporal changes. We expect VICR to achieve more stable cloud removal performance in landscapes with complex spatial pattern and abrupt change than the previous cloud removal algorithms based on temporal reference image(s). In addition, we expect that VICR is computational efficient and can be practically applied for cloud removal for time-series images.

2. Virtual image patch-based Cloud Removal (VICR) algorithm

VICR performs cloud removal for each cloud region separately. The basic idea of VICR is that Landsat SR image patch at band *n* within a cloud region can be reconstructed by a virtual image patch that is transformed from time-series reference image patches and a residual image.

$$\hat{\boldsymbol{L}}_{p\_cr}(n) = \boldsymbol{L}_{v\_cr}(n) + \boldsymbol{\gamma}_{cr}(n) \tag{1}$$

where $\hat{\boldsymbol{L}}_{p\_cr}(n)$ indicates the Landsat SR image patch within the cloud region at band *n* at target time, $\boldsymbol{L}_{v\_cr}(n)$ indicates the virtual surface reflectance image patch at band *n*, and $\boldsymbol{\gamma}_{cr}(n)$ indicates the residual image patch.

As illustrated in Fig.1, VICR includes three main steps: (1) construct the virtual image patch $\boldsymbol{L}_{v\_cr}(n)$ in the cloud region by local linear transformation of time-series reference images; in this step, the optimal set of reference images are determined (Section 2.1); (2) for each pixel in the cloud region, select similar pixels in the neighborhood of the cloud region with TWSD (Section 2.2); (3) construct residual image $\boldsymbol{\gamma}_{cr}(n)$ for cloud region based on similar pixels and then predict SR image $\hat{\boldsymbol{L}}_{p\_cr}(n)$ in the cloud region (Section 2.3).

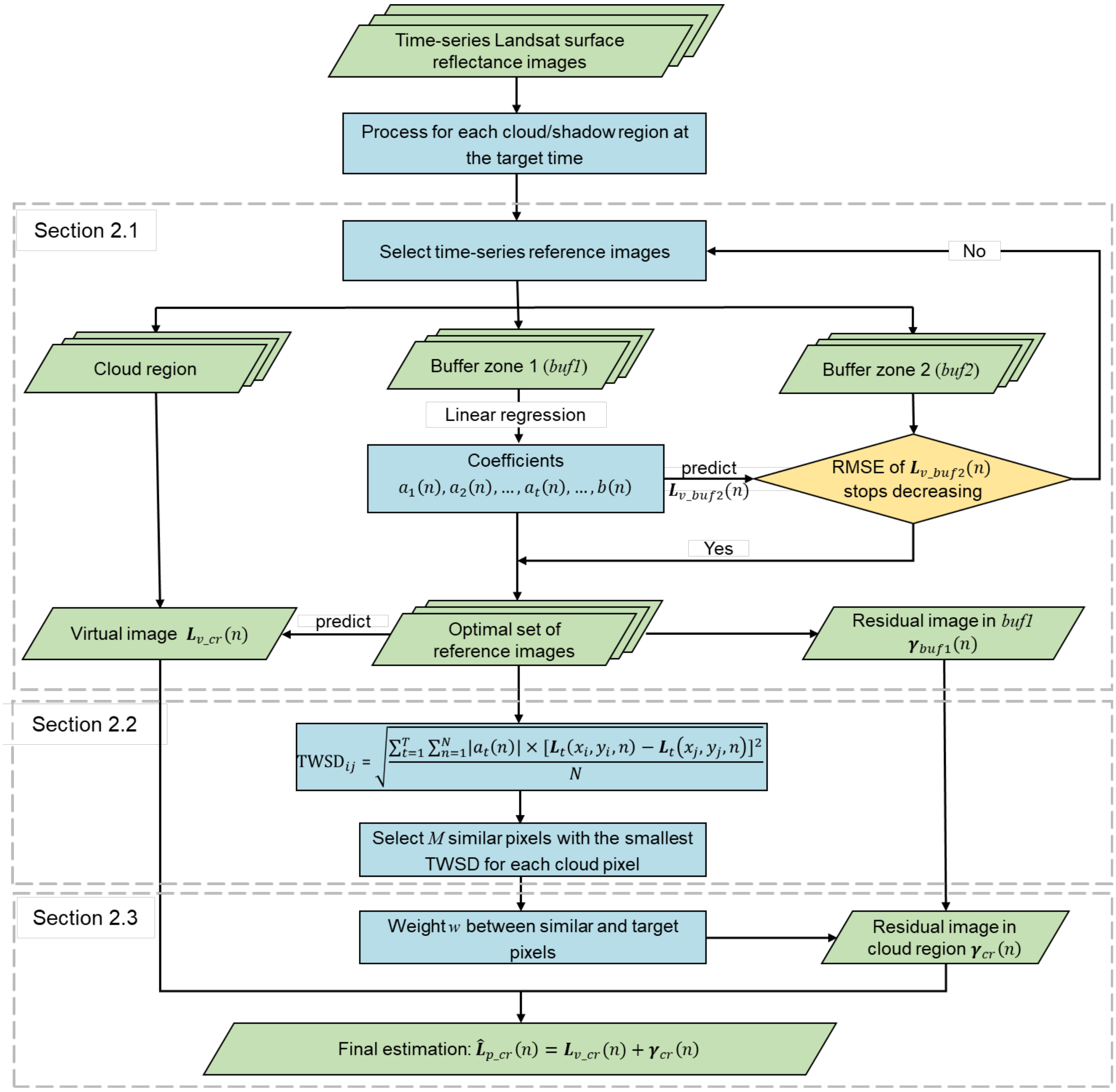

Fig. 1. The flowchart of VICR

2.1 Construct virtual image patch

VICR constructs virtual image patch within cloud region for each band. For band n, $\boldsymbol{L}_{v\_cr}(n)$ is a linear transformation of time-series reference image patches in the same region. It can be expressed as:

$$\boldsymbol{L}_{v\_cr}(n)= \sum_{t=1}^{T} a_t(n) \times \boldsymbol{L}_{t\_cr}(n) + b(n) \tag{2}$$

where $\boldsymbol{L}_{t\_cr}(n)$ is the reference image patch in the cloud region acquired at time t. Note that $\boldsymbol{L}_{t\_cr}(n)$ should be cloudless in the cloud region. T is the total number of reference images. $a_t(n)$ is the coefficient of the t^{th} reference image and $b(n)$ is a constant. Both parameters are to be estimated, and the optimal set of time-series reference image patches are to be determined.

2.1.1 Estimation of $a_t(n)$ and $b(n)$

To estimate $a_t(n)$ and $b(n)$, we assume that the image patch in the cloud region and its neighborhood image around the cloud region share the same transformation function. Therefore, we generate a buffer area outside the cloud region using dilation operation with a window size of 31×31 pixels ("imdilate" function in MATLAB). The buffer area has approximately 15 pixels width, and we call it "buffer zone 1" (*buf1*) as illustrated in Fig. 2. Next, $a_t(n)$ and $b(n)$ are estimated using the linear regression model fitted between time-series reference image patches at time t and the image patch at the target time within *buf1*.

$$\boldsymbol{L}_{buf1}(n)= \sum_{t=1}^{T} a_t(n) \times \boldsymbol{L}_{t\_buf1}(n) + b(n) + \boldsymbol{\gamma}_{buf1}(n) \tag{3}$$

where $\boldsymbol{L}_{buf1}(n)$ represents the image within *buf1* at band n at the target time, and $\boldsymbol{L}_{t\_buf1}(n)$ represents the reference image within *buf1* at band n at time t. $\boldsymbol{\gamma}_{buf1}(n)$ represents the residual image of the band n within *buf1*. $a_t(n)$ and $b(n)$ are derived using the least squares method.

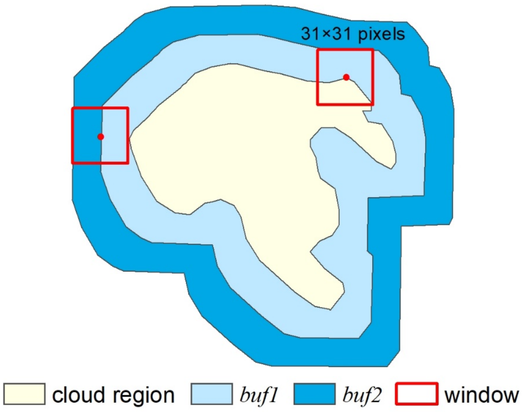

Fig. 2. Establishment of buffer zone 1 (*buf1*), buffer zone 2 (*buf2*) around the cloud region.

2.1.2 Selection of the optimal set of time-series reference images

In the above process, it is clear that the number and the acquisition time of the reference images affect the accuracy of regression fitting. We expect that a set of reference images can be selected to minimize $\boldsymbol{\gamma}_{buf1}(n)$ so that the virtual image estimated from Eq. 3 is as close as the real image at the target time. For this purpose, we build a new buffer area with the same window size outside *buf1*, which is called buffer zone 2 (*buf2*) (Fig. 2). The virtual image at the target time within *buf2* ($\boldsymbol{L}_{v\_buf2}$) is obtained through the regression parameters $a_t(n)$, $b(n)$ and the reference images within *buf2* ($\boldsymbol{L}_{t\_buf2}(n)$) (Eq. 4).

$$\boldsymbol{L}_{v\_buf2}(n)= \sum_{t=1}^{T} a_t(n) \times \boldsymbol{L}_{t\_buf2}(n) + b(n) \qquad (4)$$

We hope that $\boldsymbol{L}_{v\_buf2}$ is very close to the real image at the target time $\boldsymbol{L}_{buf2}$. We assume that the reference image patches that yield the most accurate estimation of $\boldsymbol{L}_{v\_buf2}$ result in the highest fitting accuracy in *buf1* as well as in the cloud region. We call these reference images the optimal set of reference images. In this study, we take an iterative strategy to select the optimal set of reference images.

Step 1. Select the image that is temporally closest to the target image and has no cloud/shadow in the cloud region as the first reference image (t_1 in Fig. 3). In case that two images are selected and have the same temporal interval with the target image, the image acquired before the target date is preferred as the first reference image. Then, calculate coefficients $a_1(n)$ and $b(n)$ by Eq.3.

Step 2. Calculate $\boldsymbol{L}_{v\_buf2}(n)$ using the coefficients (Eq. 4) and then calculate the root mean square error of $\boldsymbol{L}_{v\_buf2}$ averaged over all bands ($\overline{RMSE_1}$) following Eq. 5.

$$\overline{RMSE} = \frac{1}{N}\sum_{n=1}^{N}\sqrt{\frac{\sum_{k=1}^{K}(\boldsymbol{L}_{v\_buf2}(x_k,y_k,n) - \boldsymbol{L}_{buf2}(x_k,y_k,n))^2}{K}} \quad (5)$$

where (x_k, y_k) is the position of the kth pixel and K represents the total number of pixels in *buf2*. N represents the total number of image bands.

Step 3. Select another image on the opposite side of the previous reference image date on the time axis (Fig. 3). If the image is cloud free within the cloud region, then consider it as the second reference image and add it in the input of Eq. 3 (t_2 in Fig. 3); otherwise, skip it and go to the other side of the image on the time axis. Calculate $\overline{RMSE_2}$ and compare it with $\overline{RMSE_1}$. If $\overline{RMSE_2} < \overline{RMSE_1}$, repeat Step 3 until $\overline{RMSE}$ does not continue to decline. At this time, it is considered that the selected images are the optimal set of time-series reference images.

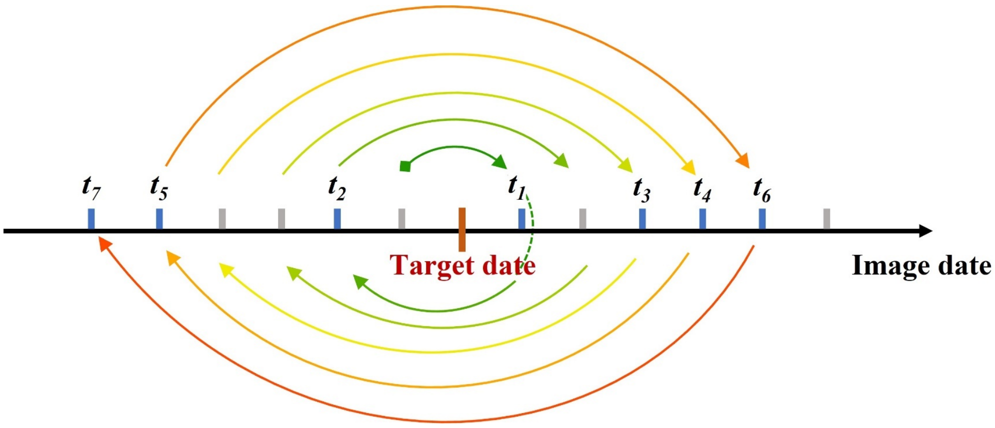

Fig. 3. An illustration of selection and sorting of reference images. The tick marks denote the image acquisition dates. The time interval between neighboring tick marks is 16 days. The red tick mark denotes

the date when the target image was acquired. The images on the grey tick marks have cloud pixels in the cloud region, therefore they are not considered as reference images. The images on the blue tick marks are cloud free within the cloud region. The arrows show the sequence of image selection. It starts from the temporally closest image before target date (shown in green square arrowhead), and then visit the image on the other side of target date. In this example, the images on t_1, t_2, …, and t_7 are added as input in sequence.

2.1.3 Generation of $\boldsymbol{L_{v\_cr}(n)}$ and $\boldsymbol{\gamma_{buf1}(n)}$

Based on the optimal set of time-series reference images, we can generate the virtual image in the cloud region at target time ($\boldsymbol{L}_{v\_cr}(n)$) using Eq. 2 and the residual image in *buf1* ($\boldsymbol{\gamma}_{buf1}(n)$) using Eq. 3.

2.2 Construct TWSD and select similar pixels

In section 2.2 and 2.3, we aim to estimate residual image $\boldsymbol{\gamma}_{cr}(n)$ for the cloud region. The residual of each pixel in the cloud region is estimated by weighted average of the residuals of its similar pixels in $\boldsymbol{\gamma}_{buf1}(n)$. To capture the change in SR in temporal domain, we propose a new similarity index, i.e., temporal-weighted spectral distance (TWSD, Eq. 6), in which both spectral and temporal distances between pixels are considered.

$$\mathrm{TWSD}_{ij} = \sqrt{\frac{\sum_{t=1}^{T}\sum_{n=1}^{N}|a_t(n)| * [\boldsymbol{L}_{t\_cr}(x_i,y_i,n) - \boldsymbol{L}_{t\_buf1}(x_j,y_j,n)]^2}{N}} \tag{6}$$

where (x_i, y_i) is the position of the ith pixel in the cloud region and (x_j, y_j) is the position of the jth pixel in *buf1*. TWSD_{ij} represents the distance between the ith pixel and the jth pixel in both spectral and temporal domain. Unlike previous spectral distance metrics (Zhu et al., 2012; Chen et al., 2017; Cao et al., 2020), we incorporate the transformation coefficient $a_t(n)$ because the magnitude of $a_t(n)$ is highly related to the correlation between the image at the reference time t and the target time. Larger $a_t(n)$ indicates higher contribution, thus the neighboring pixels at time *t* should be given greater weights. For each pixel in the cloud region, we select the 20 pixels with the lowest TWSD (i.e., $M = 20$) as the similar pixels of the target pixel. These similar pixels are used to estimate the residuals of the target pixel and then to obtain the residual image in the cloud region.

2.3 Estimate residual image and recover cloud image

For a target pixel (x_i, y_i) in the cloud region, its residual is estimated using linear weighted sum approach considering the spatial and spectral-temporal distances to its similar pixels. The spatial distance Dist_{ij} between the target pixel i and its similar pixel j is calculated as their Euclidean distance.

$$\mathrm{Dist}_{ij} = \sqrt{\left(x_i - x_j\right)^2 + \left(y_i - y_j\right)^2} \tag{7}$$

We use TWSD_{ij} to represent the spectral-temporal distance between pixel i and j. Then, Dist_{ij} and TWSD_{ij} are normalized through:

$$D_{ij} = \frac{\mathrm{Dist}_{ij} - \min(\mathrm{Dist}_i)}{\max(\mathrm{Dist}_i) - \min(\mathrm{Dist}_i)} + 1 \tag{8}$$

$$ST_{ij} = \frac{\mathrm{TWSD}_{ij} - \min(\mathrm{TWSD}_i)}{\max(\mathrm{TWSD}_i) - \min(\mathrm{TWSD}_i)} + 1 \tag{9}$$

where D_{ij} and ST_{ij} represent the normalized spatial distance and spectral-temporal distance respectively. Dist_i and TWSD_i represent the arrays composed of the spatial distances $[\mathrm{Dist}_{i1}, \mathrm{Dist}_{i2}, \ldots, \mathrm{Dist}_{iM}]$ and spectral-temporal distances $[\mathrm{TWSD}_{i1}, \mathrm{TWSD}_{i2}, \ldots, \mathrm{TWSD}_{iM}]$ between the target pixel i and the *M* similar pixels, respectively (*M*=20). The $\max(\cdot)$ and $\min(\cdot)$ are to find the maximum and minimum values of the array. The weight w_{ij} of the similar pixel j of the target pixel i is calculated as:

$$w_{ij} = \frac{1/(D_{ij} ST_{ij})}{\sum_{j=1}^{M} 1/(D_{ij} ST_{ij})} \tag{10}$$

Finally, for the cloud region we obtain the residual value of the target pixel *i* by weighted summation of the residuals of the similar pixels in *buf1*.

$$\boldsymbol{\gamma}_{cr}(x_i, y_i, n) = \sum_{j=1}^{M} w_{ij} \times \boldsymbol{\gamma}_{buf1}(x_j, y_j, n) \tag{11}$$

When the residual image of the cloud area $\boldsymbol{\gamma}_{cr}(n)$ is constructed, it is added to the virtual image $\boldsymbol{L}_{v\_cr}$ obtained in Eq. 1 to predict the cloud free image in the cloud region $\hat{\boldsymbol{L}}_{p\_cr}$. Following the above procedures, we reconstruct each cloud region separately. Once the image patches in all cloud regions are reconstructed, they are combined to obtain the final cloud-free image scene.

3. Experimental data and evaluation

3.1 Testing sites

Four sites with different landscape heterogeneities and land change patterns were selected to evaluate the VICR method. The first site is at the Jianghan Plain in Hubei Province, China (112.8°E, 30.2°N). This site is an important agricultural production area in Central China. The crop types are dominated with rapeseed and paddy rice rotations (Tao et al., 2019; Fang et al., 2021) and the croplands are fragmented, presenting heterogeneous spatial patterns. The second site is in the Lower Gwydir Catchment, Australia (149.36°E, 29.08°S). Land use include grazing, dryland cropping, horticulture, and irrigated lands (Shi et al., 2014). A flood event occurred in mid-December 2004, resulting in an abrupt land cover change shown on the Landsat 5 TM image on December 12th, 2004. The third site covers urban and suburban areas in Beijing (116.45°E, 39.95°N), China, presenting great spatial heterogeneity and vegetation phenological dynamics. The fourth site is at the coastal wetland in Yellow River Delta in Shandong Province, China (119.2°E, 37.75°N). As an area with intense land sea interactions, land surface reflectance changes frequently due to tidal inundation and sediment accumulation. In recent years, the landscape patterns in the Yellow River Delta have changed dramatically due to rapid expansion of an invasive plant species *Spartina alterniflora* (Wang et al., 2021).

3.2 Landsat data and preprocessing

To evaluate the VICR method, we selected a cloud-free Landsat imagery at each site and simulated a cloud region (hereafter we call target image) (Fig. 4). The cloud region has around 90,000~100,0000 pixels. Time-series Landsat images with cloud cover less than 80% acquired before and after the target date were considered as candidate reference images. All Landsat images were Collection 1 Tier 1 Level 2 surface reflectance products downloaded from Google Earth Engine. For each Landsat image, we used the quality assurance band to detect cloud and cloud shadow regions and mask them. We did not use Landsat 7 ETM+ images because the images had missing strips after the scan-line corrector failed in 2003.

(A) Jianghan Plain

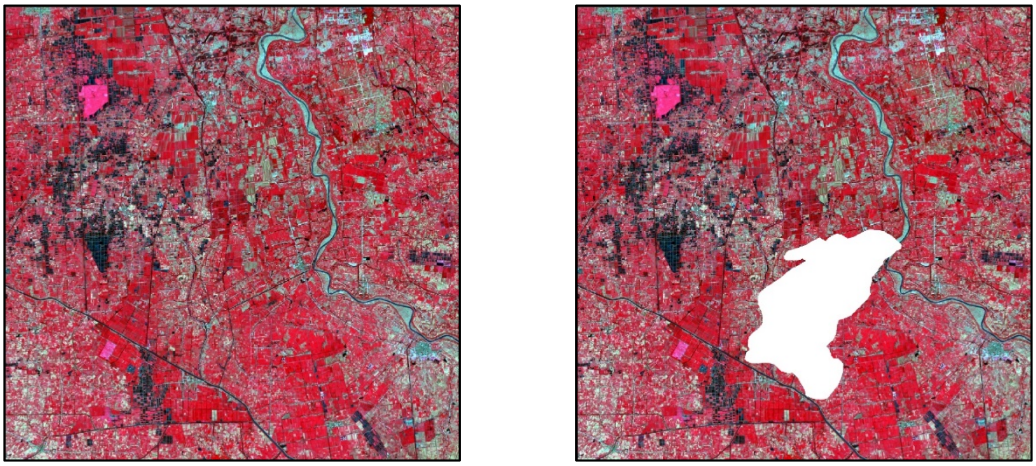

Actual image (09/14/15) Cloud-simulated image

(B) Lower Gwydir Catchment

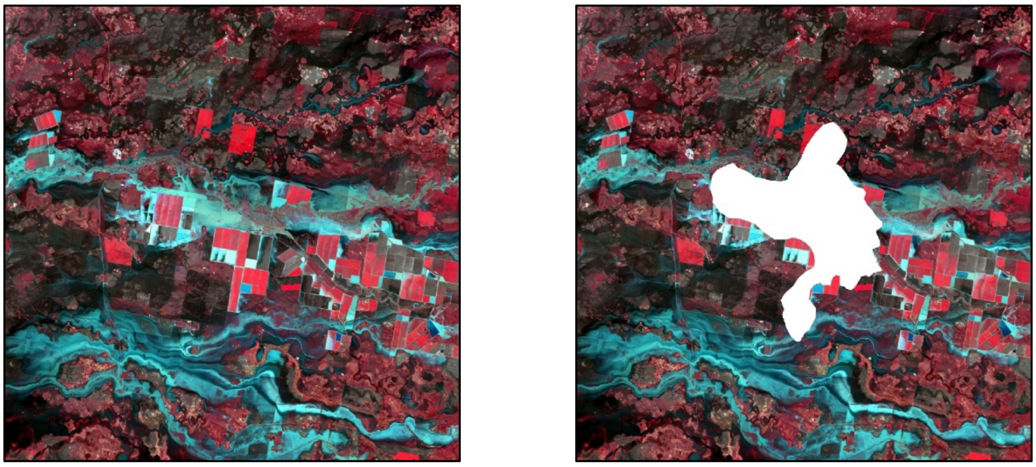

Actual image (12/12/04) Cloud-simulated image

(C) Beijing

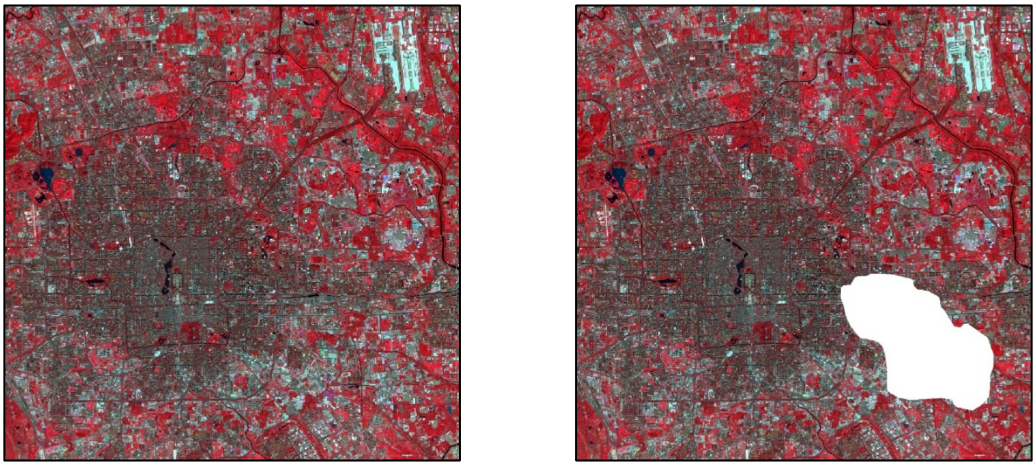

Actual image (09/12/17) Cloud-simulated image

(D) Yellow River Delta

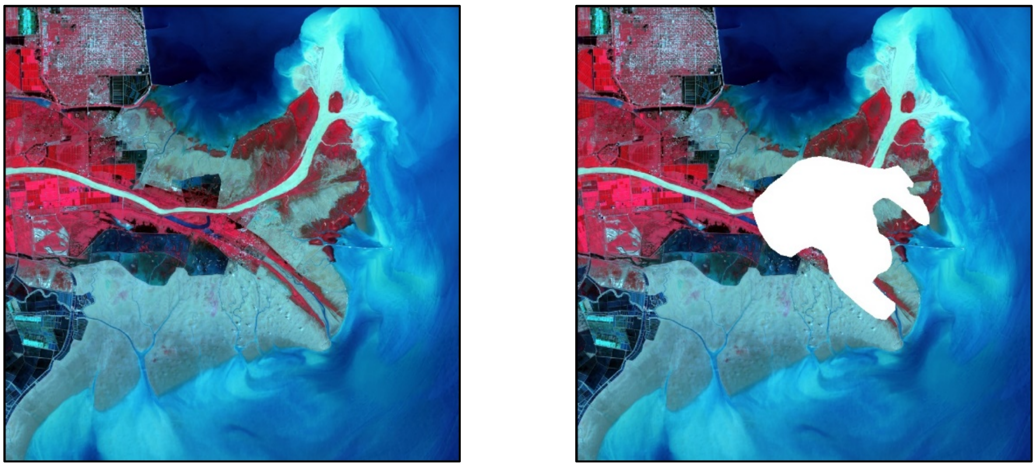

Actual image (07/31/18) Cloud-simulated image

Fig. 4. Actual images and cloud-simulated images in standard false color composition over (A) Jianghan Plain (Landsat 8 OLI), (B) Lower Gwydir Catchment (Landsat 5 TM), (C) Beijing (Landsat 8 OLI), and (D) Yellow River Delta (Landsat 8 OLI). Acquisition dates are in the parentheses in the format of MM/DD/YY.

The image sizes for the testing sites A-C are 1200×1200 pixels, and that of testing site D is 1397×1234 pixels. The number of simulated cloud pixels in (A-D) are 93312, 107529, 89813, and 103174, respectively.

3.3 Assessment metrics

The performance of VICR was evaluated by comparing the reconstructed images and the actual image in cloud region. Quantitative assessment was conducted using Correlation Coefficient (CC), Root Mean Square Error (RMSE) and Structural Similarity Index Measure (SSIM). CC represents the degree of agreement between the estimation and the real value. RMSE measures the statistical difference of pixel values between the predicted image and the real image. SSIM evaluates the overall structure similarity between the two images (Zhou et al., 2004). The quantitative evaluation was carried out for six bands of Landsat OLI/TM sensors, i.e., blue, green, red, near infrared red (NIR), short-wave infrared 1 (SWIR1) and short-wave infrared 2 (SWIR2) bands.

4. Experiment design and results

Seven experiments were designed to evaluate the performances of VICR method from multiple aspects. Experiment I (Section 4.1) aimed to verify the reliability of the automatic selection of optimal reference images. Experiment II (Section 4.2) evaluated the effectiveness of the TWSD metrics. Experiment III (Section 4.3) compared the accuracies of VICR with ARRC, mNSPI and WLR algorithms. Experiment IV (Section 4.4) evaluated the sensitivity of reconstruction accuracy to reference image compared to ARRC, mNSPI and WLR. Experiment V (Section 4.5) analyzed the influence of different cloud sizes on the stability of the accuracies. Experiment VI (Section 4.6) used real cloud-contaminated images for cloud removal and compared the reconstruction effects with ARRC, mNSPI and WLR. Meanwhile, taking

Jianghan Plain and Yellow River Delta as examples, the time-series NDVIs were constructed and compared with the NDVI from MODIS (MOD13Q1). Experiment VII (Section 4.7) compared the computation efficiencies of VICR with ARRC, mNSPI and WLR methods.

We selected mNSPI, WLR and ARRC for comparison because they all involved using both temporal and spatial auxiliary information in reference image(s) for cloud removal. mNSPI and WLR are based on a single reference image and have been widely used. The source codes are publicly available (mNSPI: https://xiaolinzhu.weebly.com/; WLR: http://sendimage.whu.edu.cn/send-resource-download/). mNSPI is provided in IDL code, and WLR is provided with an executable program. ARRC is a recently proposed cloud removal method based on time series Landsat images (Cao et al., 2020). It combines predictions from a long-term component using autoregression of time series observations (3 years of Landsat images were used as recommended by ARRC) and a short-term component based on a single cloudless reference image. As the source code is not available, we rewrote ARRC on MATLAB. VICR was also coded on MATLAB. All processes in this study were carried out on a workstation (Dell-T8520, CPU: i9-10900X 3.70GHz, RAM: 32GB).

4.1 Experiment I: Assessment on the selection of optimal set of reference images

4.1.1 Experiment design

VICR uses the fitting parameters obtained from *buf1* to predict virtual image in *buf2* ($\boldsymbol{L}_{v\_buf2}$) at the target time, and the RMSE between the $\boldsymbol{L}_{v\_buf2}$ and the actual image in *buf2* ($\boldsymbol{L}_{buf2}$) was used to guide determination of the optimal set of time-series reference images. The basic assumption is that with changing reference images the prediction errors in the cloud region present the same variation patterns as the $\overline{RMSE}$s of $\boldsymbol{L}_{v\_buf2}$, because *buf2* and the cloud region are spatially close. To justify the assumption, we conducted VICR based on the input of 1 to 12 reference images. The reference images were selected and added to the reference image list following the procedures in Section 2.1 (Fig. 3), and the order of the input images is shown in Table 1. The $\overline{RMSE}$ of $\boldsymbol{L}_{v\_buf2}$, the $\overline{RMSE}$ of the virtual image in the cloud region ($\boldsymbol{L}_{v\_cr}$), and the $\overline{RMSE}$ of the reconstructed image in the cloud region ($\hat{\boldsymbol{L}}_{p\_cr}$) were calculated for four testing sites, respectively.

Table 1. Reference images and their input orders for VICR in Jianghan Plain, Lower Gwydir Catchment, Beijing and Yellow River Delta.

Jianghan Plain		Lower Gwydir Catchment		Beijing		Yellow River Delta	
Reference image	Order	Reference image	Order	Reference image	Order	Reference image	Order
11/14/14	11	08/06/04	11	03/04/17	11	05/25/17	12
12/16/14	10	08/22/04	10	04/21/17	8	07/12/17	10
01/17/15	8	09/23/04	8	05/07/17	6	09/30/17	9
03/22/15	6	10/09/04	6	05/23/17	4	01/20/18	6
07/28/15	3	10/25/04	4	07/10/17	2	03/09/18	5
Target image: 09/14/15		11/26/04**	1	**Target image: 09/12/17**		06/29/18**	2
10/16/15*	1	**Target image: 12/12/04**		09/28/17*	1	**Target image: 07/31/18**	
11/01/15**	2	12/28/04*	2	10/30/17**	3	08/16/18*	1
02/05/16	4	01/13/05	3	11/15/17	5	09/17/18	3
05/11/16	5	01/29/05	5	12/01/17	7	10/03/18	4
04/09/16	7	02/14/05	7	12/17/17	9	03/12/19	7
08/31/16	9	03/02/05	9	01/02/18	10	04/13/19	8
12/05/16	12	04/03/05	12	02/03/18	12	05/31/19	11

Image date in MM/DD/YY

* represents the cloudless reference image for mNSPI, WLR and ARRC short-term components in Experiment III.

** represents the cloudless reference image for mNSPI, WLR and ARRC short-term components when the image * is not available in Experiment IV.

4.1.2 Experiment results

In general, the $\overline{RMSE}$s of $\boldsymbol{L}_{v\_buf2}$, $\boldsymbol{L}_{v\_cr}$ and $\hat{\boldsymbol{L}}_{p\_cr}$ show consistent pattern with increasing number of reference images (Fig. 5). They all present decreasing trend with first a few reference images and then gradually stabilize. For Beijing, the $\overline{RMSE}$s of $\boldsymbol{L}_{v\_buf2}$, $\boldsymbol{L}_{v\_cr}$ and $\hat{\boldsymbol{L}}_{p\_cr}$ all reach the minimum when 3 reference images were used as input (Fig. 5c). For

Jianghan Plain, Lower Gwydir Catchment and Yellow River Delta, the $\overline{RMSE}$ of $\boldsymbol{L}_{v\_buf2}$ stops decreasing when the 7th, 6th and 6th reference image was added, respectively (Fig. 5a, b, d). This means that the first 7, 6, and 6 images were selected as the optimal set of reference images for the three sites, respectively. With these reference images, unfortunately, the $\overline{RMSE}$ of $\hat{\boldsymbol{L}}_{p\_cr}$ are not the minimum. For Jianghan Plain, Lower Gwydir Catchment and Yellow River Delta, the $\overline{RMSE}$ of $\hat{\boldsymbol{L}}_{p\_cr}$ reaches the minimum with 4, 11 and 10 reference images, respectively (Figure 5a, b, d). However, little difference is found between the minimum $\overline{RMSE}$ and the $\overline{RMSE}$ resulted from the optimal set of reference images (1.43×10^{-4} for Jianghan Plain, 0.3×10^{-4} for Beijing, and 4.5×10^{-4} for Yellow River Delta), indicating that good accuracies are still achieved with the optimal set of reference images.

Fig. 5 shows that the first a few reference images temporally close to the target date had more contribution than those images farther from the target date. The $\overline{RMSE}$s first decreased substantially and then had little change or even increased slightly. It seems that more reference images do not necessarily lead to higher accuracies. For instance, for Beijing the $\overline{RMSE}$s of $\hat{\boldsymbol{L}}_{p\_cr}$ show slight increase when more than 3 reference images were used as input; for Lower Gwydir Catchment, the $\overline{RMSE}$ from 12 reference images is higher than that from 6 and 11 reference images. In addition, we observe that the $\overline{RMSE}$ of $\hat{\boldsymbol{L}}_{p\_cr}$ is much lower than that of $\boldsymbol{L}_{v\_cr}$ regardless of the number of reference images, suggesting that the estimation of residual image based on similar pixels is critical for the estimation of $\hat{\boldsymbol{L}}_{p\_cr}$.

374 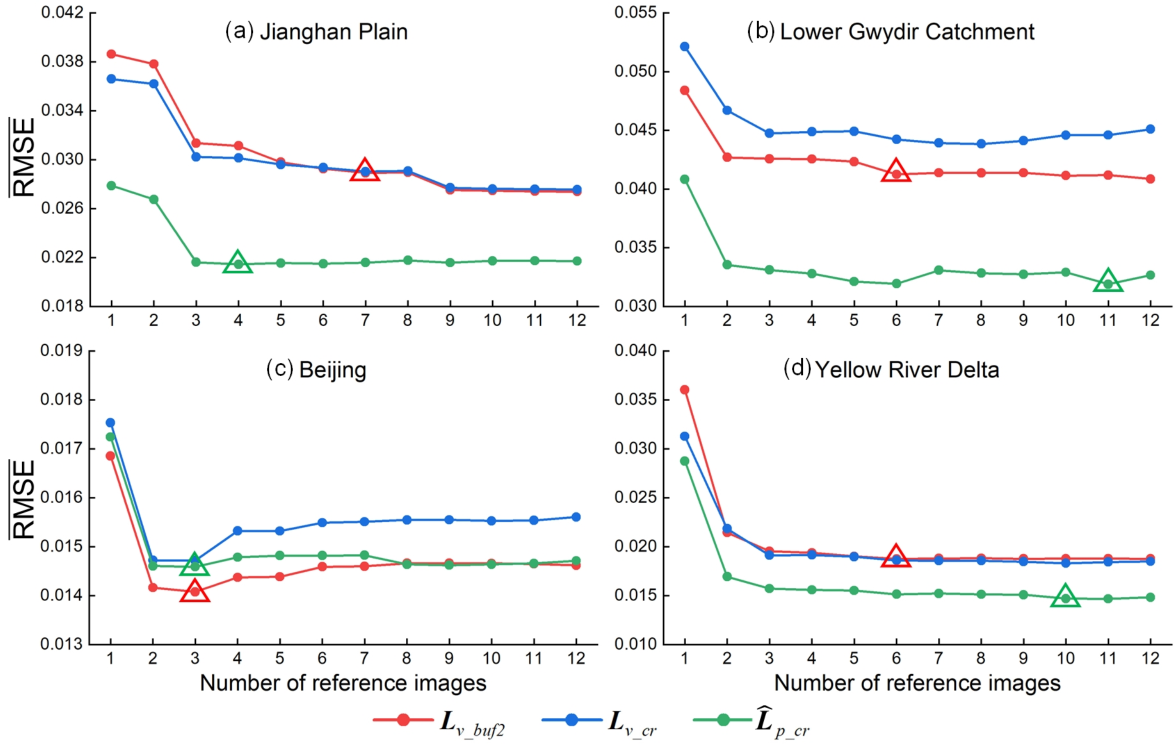

375 Fig. 5. $\overline{RMSE}$s of the virtual image in the buffer zone 2 ($\boldsymbol{L}_{v_buf2}$), the virtual image in the cloud region

376 ($\boldsymbol{L}_{v\_cr}$), and the reconstructed image in the cloud region $\hat{\boldsymbol{L}}_{p\_cr}$ resulted from one to twelve reference

377 images. The minimum RMSEs of $\boldsymbol{L}_{v\_buf2}$ and $\hat{\boldsymbol{L}}_{p\_cr}$ are marked with triangles.

378 ## 4.2 Experiment II: Assessment on TWSD

379 ### 4.2.1 Experiment design

380 VICR uses TWSD to select similar pixels in *buf1* and to estimate residuals for the target

381 pixels in cloud region. The newly proposed TWSD considers the spectral similarity between

382 pixels in temporal domain. To test the efficacy of TWSD, we compared the TWSD to spectral

383 distance (SD) that has been widely used for similar pixel selection in cloud removal algorithms

384 such as NSPI, mNSPI, STWR and the ARRC short-term component. Apart from similar pixel

385 selection, these algorithms also used SD to quantify the contribution of the similar pixels to

386 the target pixel. In this experiment, we designed four scenarios.

Scenario 1: SD is used for both similar pixel selection and residual allocation (substitute TWSD in Eq. 9 with SD) based on virtual images in cloud region and *buf1*. The formulation of SD is listed in Eq. 12.

Scenario 2: SD is used to select similar pixels, and TWSD is used to allocate residuals.

Scenario 3: TWSD is used to select similar pixels, and SD is used to allocate residuals.

Scenario 4: TWSD is used for both similar pixel selection and residual allocation (VICR).

$$SD_{ij} = \sqrt{\frac{\sum_{n=1}^{N}[\boldsymbol{L}_{v\_cr}(x_i,y_i,n) - \boldsymbol{L}_{v\_buf1}(x_j,y_j,n)]^2}{N}} \quad (12)$$

For each site and each band of Landsat image, the cloud-removed image in cloud region was compared with the actual image, and RMSE was calculated. By comparing the RMSEs of reconstruction results, the role of TWSD in similar pixel selection and residual redistribution is analyzed.

4.2.2 Experiment results

Fig. 6 shows that TWSD for both similar pixel selection and residual allocation (Scenario 4) achieved the lowest RMSE for the four testing sites (except for the NIR and SWIR1 image in Beijing), while Scenario 1 produced the highest RMSE. When TWSD was used for similar pixel selection (Scenario 3 and 4), the reconstruction accuracies were significantly improved regardless which metrics was used for residual allocation (Scenario 3 vs. Scenario 1; Scenario 4 vs. Scenario 2). When SD was used for similar pixel selection, TWSD used for residual estimation slightly improved the reconstruction accuracy (Scenario 2 vs. Scenario 1). Compared to the other three testing sites, the Lower Gwydir Catchment which experienced abrupt land change witnessed greater accuracy improvement when TWSD was used for similar pixel selection (Fig. 6b). This suggests that the similarity between similar pixels and target pixels plays a critical role in reconstruction, especially for the images with great land change.

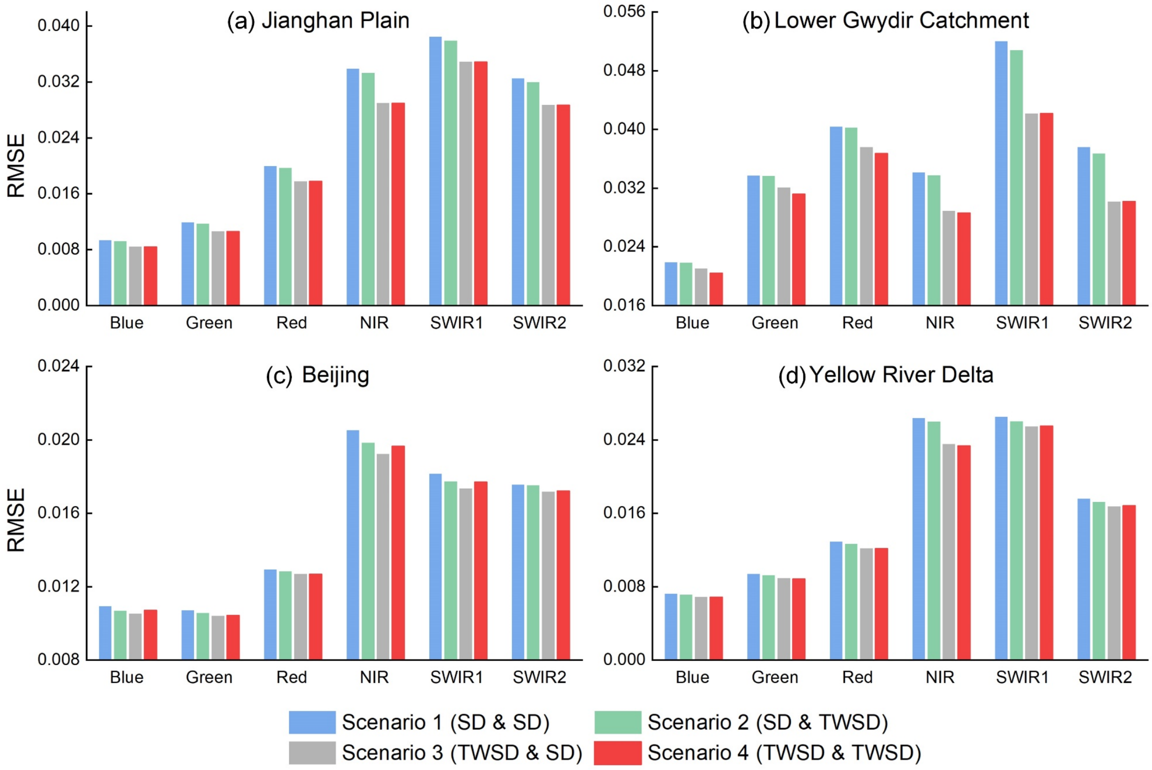

Fig. 6. RMSEs of the reconstructed cloud image at each band for (a) Jianghan Plain, (b) Lower Gwydir Catchment, (c) Beijing and (d) Yellow River Delta at four scenarios where spectral distance (*SD*) and/or temporally weighted spectral distance (TWSD) for similar pixel selection and/or residual allocation.

4.3 Experiment III: Quantitative evaluation and comparison with other cloud-removal methods

4.3.1 Experiment design

To evaluate the performance of VICR, we compared the reconstruction accuracies of VICR with those of mNSPI, WLR and ARRC. We conducted two sub-experiments. The first one was performed on the cloud-simulated images in Table 1. For mNSPI, WLR, and ARRC short-term component, we used the cloud free image that was closest to the cloud contaminated image as reference image (Table 1, Fig. S1). The second sub-experiment was performed for each site on another cloud simulated image (Table S1). On these images, three cloud regions with a total of over 120, 000 pixels were generated and randomly distributed across the image (Fig. S2). For both sub-experiments, 20 similar pixels were selected for VICR, mNSPI, WLR and ARRC short-term component for fair comparison. CC, RMSE and SSIM were calculated for the cloud regions and used as quantitative metrics. For the second sub-experiment, the values of the quantitative metrics for each cloud region were averaged.

4.3.2 Experiment results

Due to space limitation, the results of the second sub-experiment are shown in supplementary materials (Fig. S2 and S3). Here we display the results of the first sub-experiments. Generally, the reconstructed images from VICR are visually more similar to the actual image than those from mNSPI, WLR and ARRC (Fig. 7). For example, for the patchy croplands in Jianghan Plain, the cloud-removed images from WLR and ARRC show poorer spatial heterogeneities and obviously smoother effects than VICR. Some fallow croplands are not well reconstructed. Both VICR and mNSPI better restore spatial details, while VICR obviously show higher spectral similarities with the actual image. For Lower Gwydir Catchment site where flooding caused significant land cover change, the cloud-removed images from mNSPI, WLR and ARRC are more similar to the reference image (Fig. S1). In comparison, the predicted image from VICR shows better spectral similarity with the actual image in part of the flood-inundated region. For Beijing site where the land change in urban areas is relatively small, the results from the four methods are close. For the Yellow River Delta, the results from mNSPI, WLR and ARRC demonstrate obvious spectral and texture discrepancies from the actual image and the tidal creeks were not well restored. In contrast, VICR generated more visually satisfactory results where tidal creeks and tidal flats are kept intact.

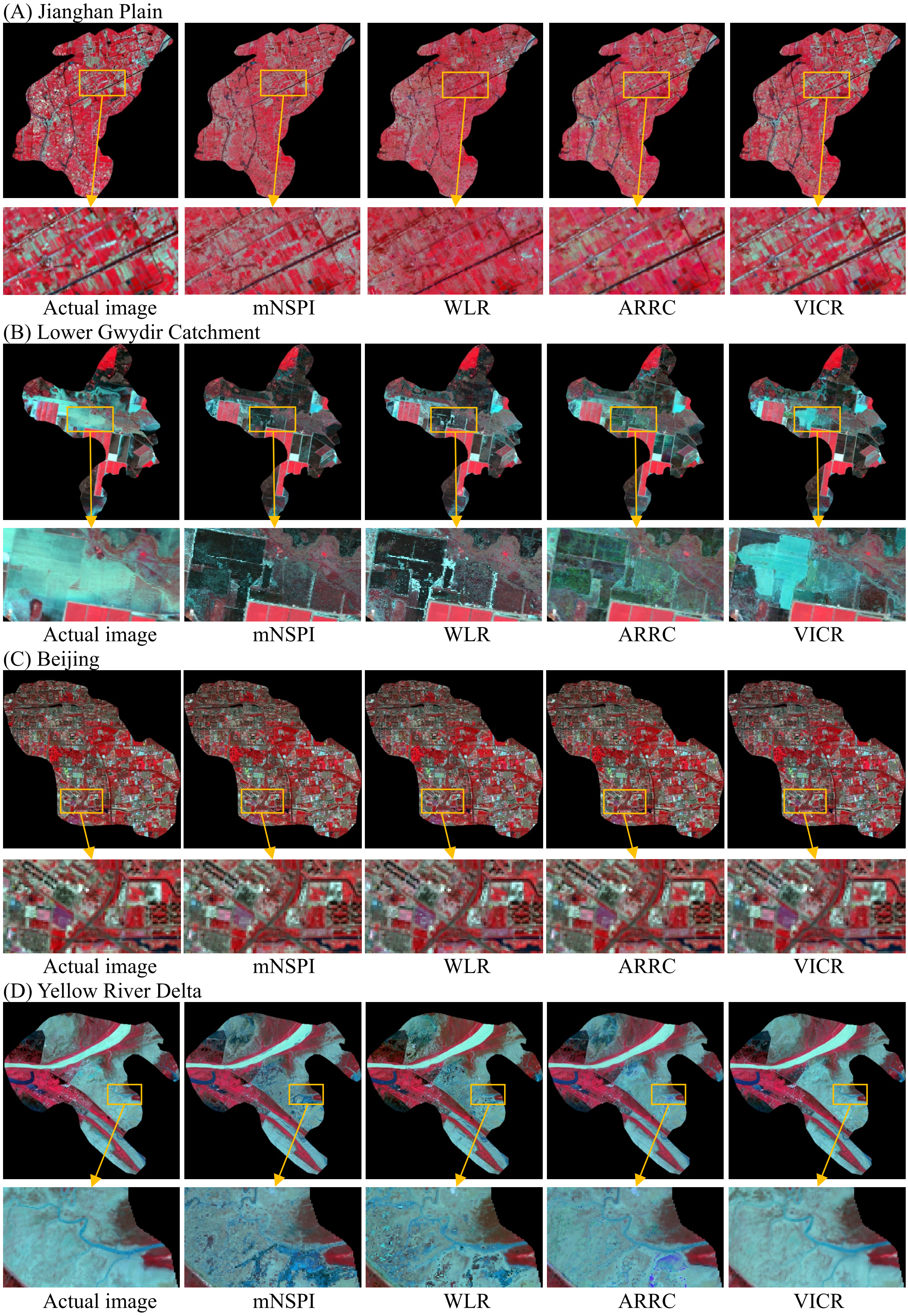

Fig. 7. Visual comparisons between mNSPI, WLR, ARRC, and VICR the cloud-simulated images over (A) Jianghan Plain, (B) Lower Gwydir Catchment, (C) Beijing and (D) Yellow River Delta.

Quantitative assessment results are shown in Fig. 8. In general, VICR presents much better performances (lower RMSE, higher CC and SSIM) than mNSPI and WLR for all sites at all bands. The decrease in RMSEs ranges from 0.0014 to 0.0223 compared to mNSPI, and ranges from 0.0017 to 0.0193 compared to WLR. For all sites, VICR performs better than ARRC in terms of CCs and RMSEs, especially for the sites with abrupt land change. For Lower Gwydir Catchment, VICR shows considerably higher CCs and lower RMSEs at red (0.0368 vs. 0.0400), green (0.0312 vs. 0.0334), SWIR1 (0.0422 vs. 0.0463) and SWIR2 (0.0302 vs. 0.0342) bands, indicating that VICR better captured the flood inundation than ARRC (Fig. 8B). At the SWIR1 and SWIR2 bands, VICR showed higher SSIMs than ARRC. For the Yellow River Delta, the improvements in CCs and RMSEs are more significant compared to the other sites. For example, CCs of VICR at NIR, SWIR1 and SWIR2 bands are 0.9507, 0.9221 and 0.9124, respectively, while those of ARRC are 0.9260, 0.8995 and 0.8962. The RMSEs of VICR at NIR, SWIR1 and SWIR2 bands are 0.0234, 0.0255 and 0.0169 respectively, while those of ARRC are 0.0286, 0.0290 and 0.0185, respectively. In most cases, VICR achieved comparable or slightly higher SSIM than ARRC. For Beijing and Jianghan Plain, VICR produced slightly lower SSIMs than ARRC at SWIR1 and SWIR2 bands (Fig. 8A and 8C). Take Beijing for example, SSIM values of ARRC at SWIR1 and SWIR2 bands are 0.9485 and 0.9514 respectively, while those of VICR are 0.9454 and 0.9485 respectively. The second sub-experiments obtained similar comparison results as the first sub-experiment (Fig. S2 and S3), and VICR achieved higher SSIM at SWIR1 and SWIR2 bands than ARRC in Jianghan Plain.

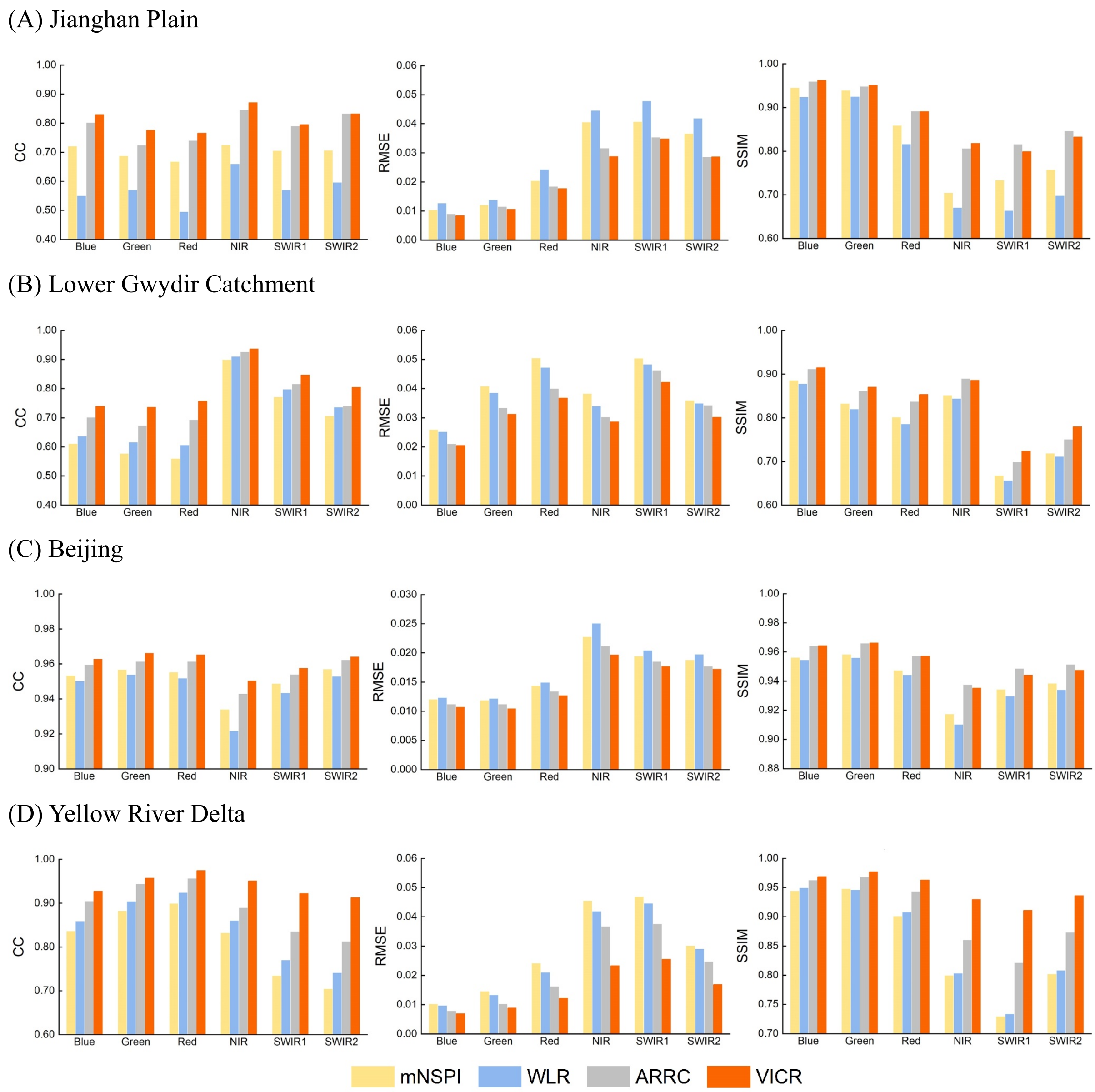

Fig. 8. Comparisons of CC (left column), RMSE (center column) and SSIM (right column) between mNSPI, WLR, ARRC, and VICR for the cloud-simulated images over (A) Jianghan Plain, (B) Lower Gwydir Catchment, (C) Beijing and (D) Yellow River Delta.

4.4 Experiment IV: Sensitivity to reference images

4.4.1 Experiment design

We hope that a robust cloud removal method is little affected by the selection of reference images. To evaluate the sensitivity of mNSPI, WLR, ARRC and VICR to different reference images, we conducted two sub-experiments by altering reference images and analyzing the change in reconstruction performances. The first sub-experiment assumes that the reference images in Experiment III were not available. For mNSPI, WLR and ARRC short-term component, we replaced the reference image in Experiment III (images with * in Table 1 and Fig. S1) with another cloud-free image (images with ** in Table 1 and Fig. S1). For ARRC long-term component and VICR, we removed the reference image from the time-series reference image list. Note that the time intervals between the target image and the new reference image were longer than or same as the original reference image. In the second sub-experiment, we assume the revisit period of Landsat satellite is 32, 48 and 64 days and thus lengthened the time interval between the reference image and the target image, and among the time-series reference images. For each site we predicted the image in the cloud region and compared the performances of the four algorithms.

4.4.2 Experiment results

Fig. 9 displays the results from the first sub-experiment. In Jianghan Plain, Lower Gwydir Catchment and Beijing, the RMSEs from all algorithms increased at most bands when using the new reference image (Fig. 9). Compared to mNSPI and WLR, ARRC and VICR obviously showed smaller increment of RMSEs, especially at the SWIR1 and SWIR2 bands for Lower Gwydir Catchment, and at all bands for Beijing. For the Beijing site, assuming that the reference image on 09/28/17 (MM/DD/YY) was not available, the next available reference image was on 10/30/17. From the target date (09/12/17) to the end of October, the land surface reflectance has changed a lot due to crop harvesting and vegetation phenological change (Figure S1A). In Lower Gwydir Catchment, although the time intervals between the two reference images (11/26/04 and 12/28/04) and the target image (12/12/04) were both 16 days, the accuracies of mNSPI and WLR decreased significantly because flood event occurred during mid-December. This indicates that large surface reflectance change has substantial negative effects on the performances of mNSPI and WLR.

In Yellow River Delta, it is interesting that using the reference image temporally farther from the target date (more than a month from 06/29/18 to 07/31/18) achieved better performance than the original reference image (08/16/18) for all methods. mNSPI, WLR and ARRC all showed considerable decrease in RMSEs at all bands, while the VICR presented more stable performance. Examination of the reference images showed that the wetlands in this site experienced tidal inundation due to high tide level on 08/16, resulting in great surface reflectance change. The reference image on 06/29 is spectrally more like the target image. Although ARRC long-term component utilized time-series Landsat images, its short-term component is still based on a single reference image. When surface reflectance experienced abrupt change, the short-term component is given higher weight when combining with long-term components (Cao et al., 2020). As a results, changing the reference image still has considerable impacts on the accuracies of ARRC in the cases where surface reflectance has abrupt change. Compared to ARRC, the change in RMSEs of VICR is negligible in Yellow River Delta (Fig. 9d). In addition, even if the time interval between the reference image and the target image becomes longer, the VICR still ensures the lowest RMSE compared to other methods for all four sites.

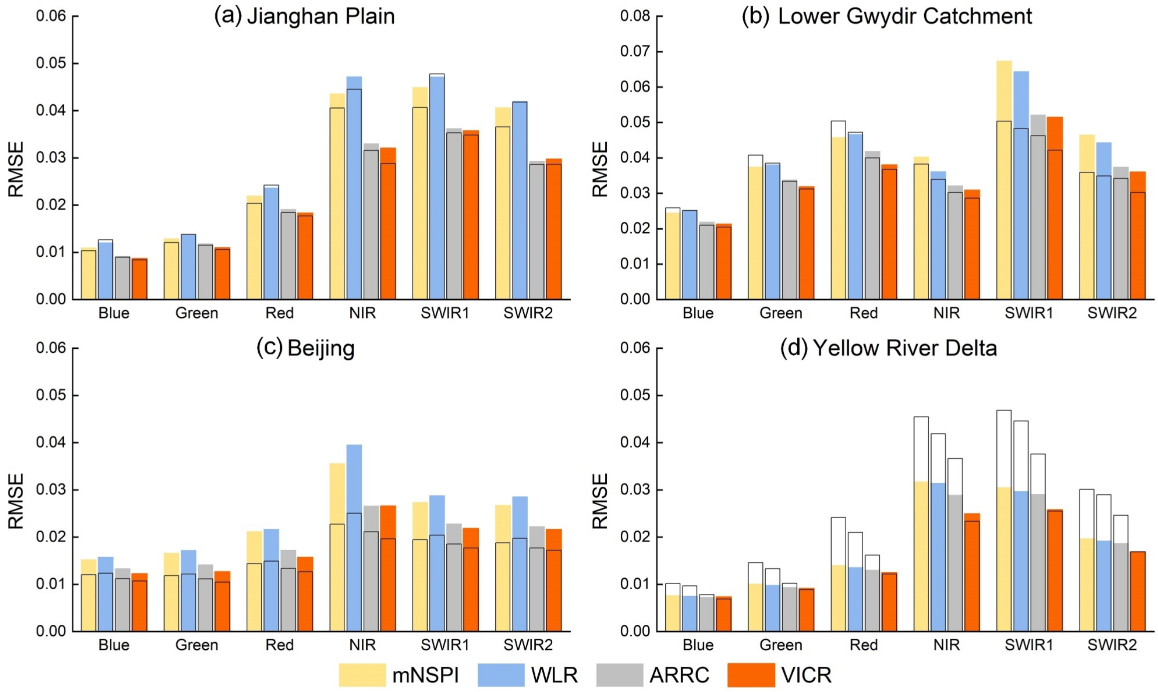

Fig. 9. Comparisons of RMSEs between mNSPI, WLR, ARRC and VICR for the cloud-simulated images for (a) Jianghan Plain, (b) Lower Gwydir Catchment, (c) Beijing and (d) Yellow River Delta in Experiment IV (colored bars) and in Experiment III (transparent bars with black border).

Fig. 10 shows the RMSEs averaged over all bands ($\overline{\text{RMSE}}$) from the second sub-experiment. All four algorithms showed increasing $\overline{\text{RMSE}}$ with increasing time intervals among images, while VICR generally showed lower magnitude of $\overline{\text{RMSE}}$ variation (except at Jianghan Plain). The reconstruction errors of VICR are significantly lower than mNSPI and WLR, and slightly lower than ARRC (except for revisit cycle = 32 days at Jianghan Plain). In Lower Gwydir Catchment and Yellow River Delta, VICR presents obvious improvement in accuracies (Fig. 10b and 10c).

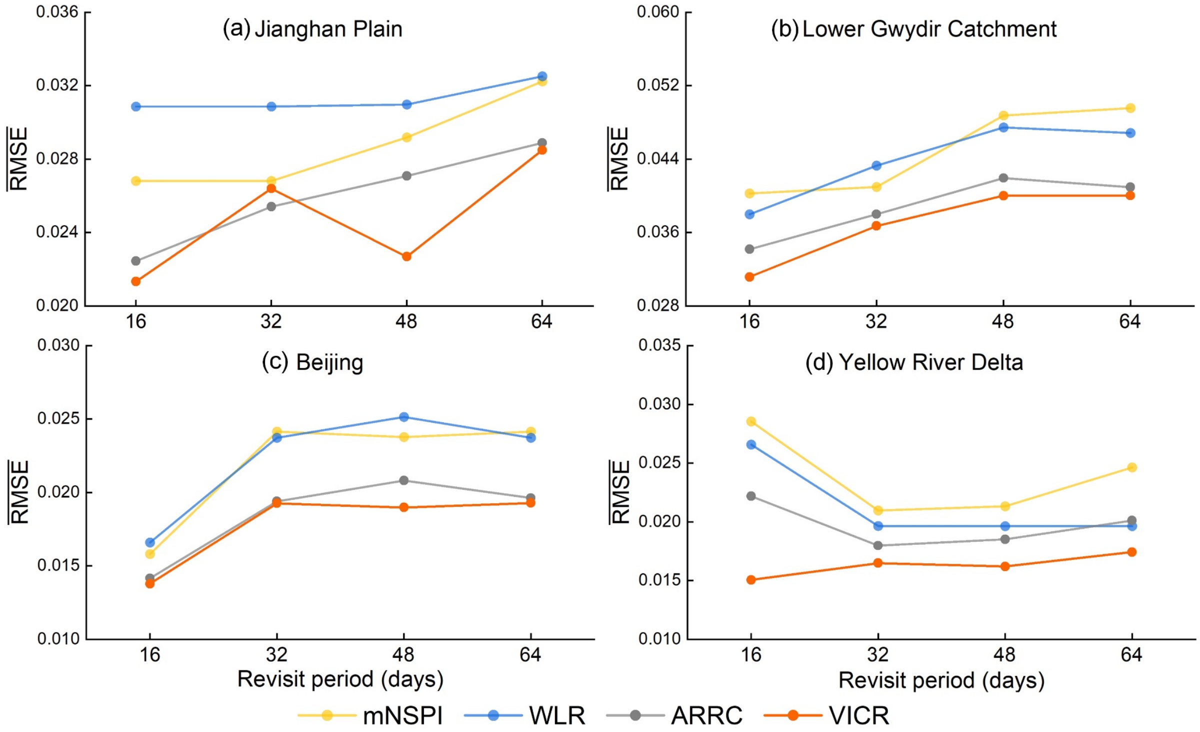

Fig. 10. Comparisons of $\overline{\text{RMSE}}$s between mNSPI, WLR, ARRC and VICR for the cloud-simulated images for (a) Jianghan Plain, (b) Lower Gwydir Catchment, (c) Beijing and (d) Yellow River Delta with revisit periods of 16, 32, 48 and 64 days.

4.5 Experiment V: Sensitivity to different cloud sizes

4.5.1 Experiment design

Intuitively, larger cloud region suggests less auxiliary information in the surrounding area can be provided for the reconstruction, especially for the central area of the cloud region. We hope that a robust cloud removal algorithm is affected by different cloud sizes as little as possible. To evaluate the sensitivity of VICR to different cloud sizes, we generated clouds with sizes of 50×50, 100×100, 150×150, 250×250, 300×300, 350×350 and 400×400 pixels (Fig. 11) and reconstructed images in the cloud region based on the same reference images in Experiment III. For each method and cloud size, RMSEs at each band in the center 50×50 pixels was calculated and compared. Note that for Yellow River Delta, we used the image on 06/29/18 as reference image for mNSPI, WLR and ARRC short-term component to avoid the impacts of tidal inundation and to ensure good results.

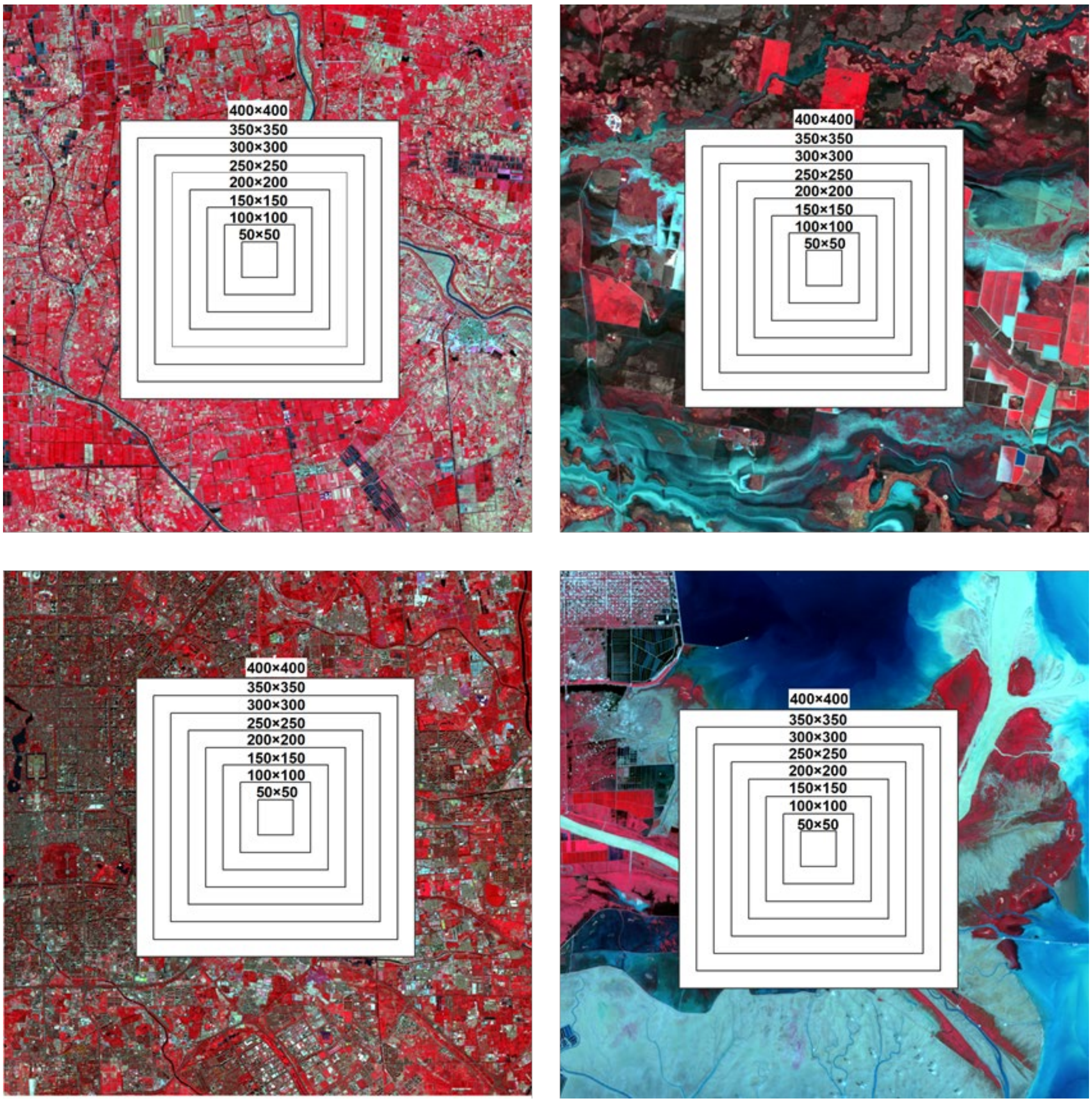

Fig. 11. Simulated clouds with 50×50, 100×100, 150×150, 250×250, 300×300, 350×350 and 400×400 pixels on the actual image in the four sites.

4.5.2 Experiment results

Fig. 12 illustrates RMSEs at NIR band of the four methods for different cloud sizes. RMSEs at other bands are shown in Fig. S4-S8 due to space limitation. VICR achieved considerably lower RMSE than mNSPI and WLR at all bands regardless of the cloud size for Jianghan Plain, Beijing and Yellow River Delta. In most cases, VICR presented slightly lower

RMSEs than ARRC. In addition, RMSEs of VICR showed smaller fluctuations than ARRC with varying cloud sizes. This is particularly noticeable at NIR band in Lower Gwydir Catchment (Fig. 12b), and at SWIR1 and SWIR2 bands in Yellow River Delta (Fig. S6). In Lower Gwydir Catchment, the RMSEs of all algorithms show upward trend with increasing cloud size (Fig. 12b). As the cloud covers the area with flood inundation, smaller cloud region indicates more flood-inundated neighboring pixels can be found. In an extreme case that the cloud covers the entire flood-inundated area, none of the neighboring pixels are spectrally similar to the target region, which certainly results in low reconstruction accuracies. Compared to mNSPI and WLR, VICR presented smaller increment of RMSE at SWIR1 and SWIR2 bands (Fig. S6), which are both representative bands showing water signal. Likewise, in Yellow River Delta, VICR achieved noticeably lower and more stable RMSEs than other methods at SWIR1 and SWIR2 bands for all cloud sizes.

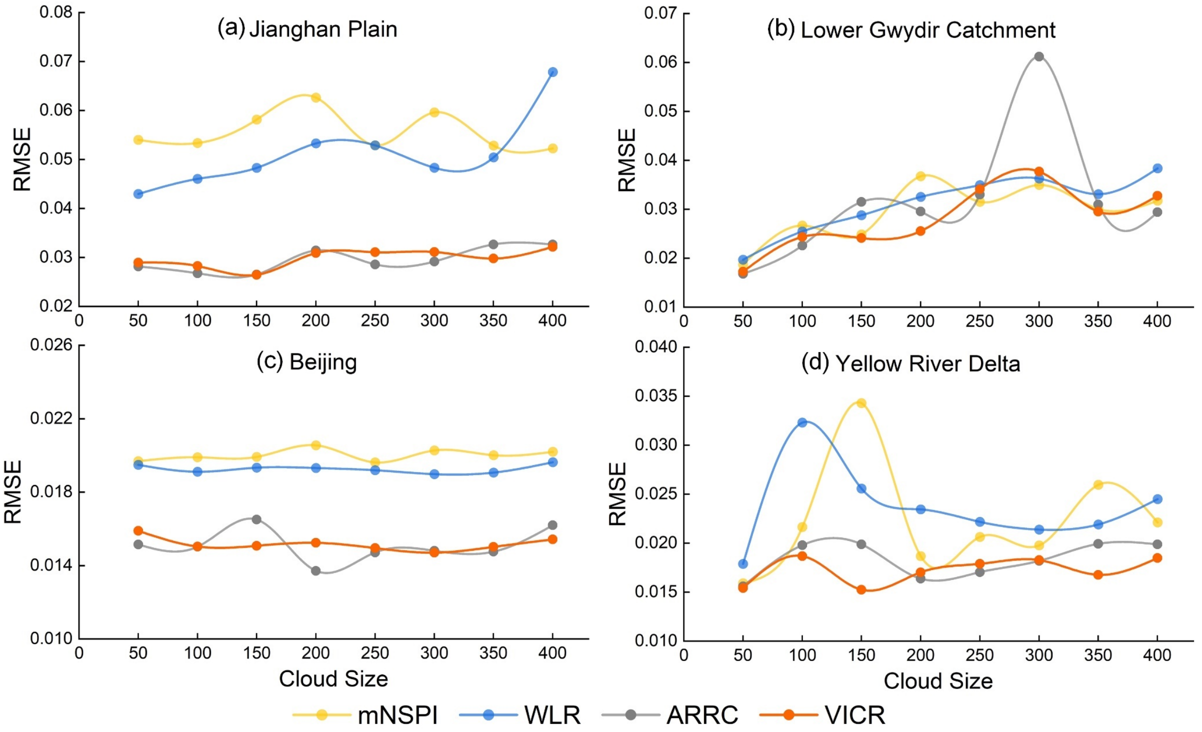

Fig. 12. The RMSEs of the reconstructed images from mNSPI, WLR, ARRC, and VICR at NIR band for

cloud sizes ranging from 50×50 pixels to 400×400 pixels. Note that the RMSEs were calculated for the 50×50 pixels in the center of the clouds.

4.6 Experiment VI: Performance on real cloud-contaminated images

4.6.1 Experiment design

In this experiment, we performed cloud removal for real cloud-contaminated images and visually compared the reconstruction results of different methods. Considering practical applications, we also used VICR to remove clouds on the time-series Landsat 8 OLI SR images during 2015-2019 at Jianghan Plain and during 2016-2020 at Yellow River Delta. We calculated Normalized Difference Vegetation Index (NDVI) based on each reconstructed image and compared the time series NDVIs with the NDVIs from the Terra Moderate Resolution Imaging Spectroradiometer (MODIS) Vegetation Indices Version 6 product (MOD13Q1). We sorted the time-series Landsat images in order of the cloud cover percentage and processed them one by one from low to high cloud cover. Each cloud-removed image was then used as the reference image for images with larger cloud cover. We call this process "time-series cloud removal procedure".

4.6.2 Experiment results

As illustrated in Fig. 13, the images reconstructed by VICR generally recovered better spatial details and maintained more realistic spectral characteristics compared to other algorithms. In Jianghan Plain, the reconstructed image by VICR presents greater spectral heterogeneity in cropland patches compared to other algorithms. The boundaries between the cropland patches are more visible in the image reconstructed by VICR. In Lower Gwydir Catchment, the images reconstructed by VICR, mNSPI and WLR presented similar spatial details, while that by ARRC presented smoother effect. In Yellow River Delta, it is obvious that the QA band layer detected larger clouds/cloud shadow areas than those in the actual image. The zoomed-in actual image covers a *Spartina Alterniflora* patch (Wang et al., 2021) which is partially contaminated by clouds in the southern coast of Yellow River Delta (yellow box in Fig.13D). The reconstructed image by VICR restores more accurate spectral information than the other methods as it is spectrally more similar to the actual image.

(A) Jianghan Plain, Landsat 8 OLI SR image acquired on 11/06/17

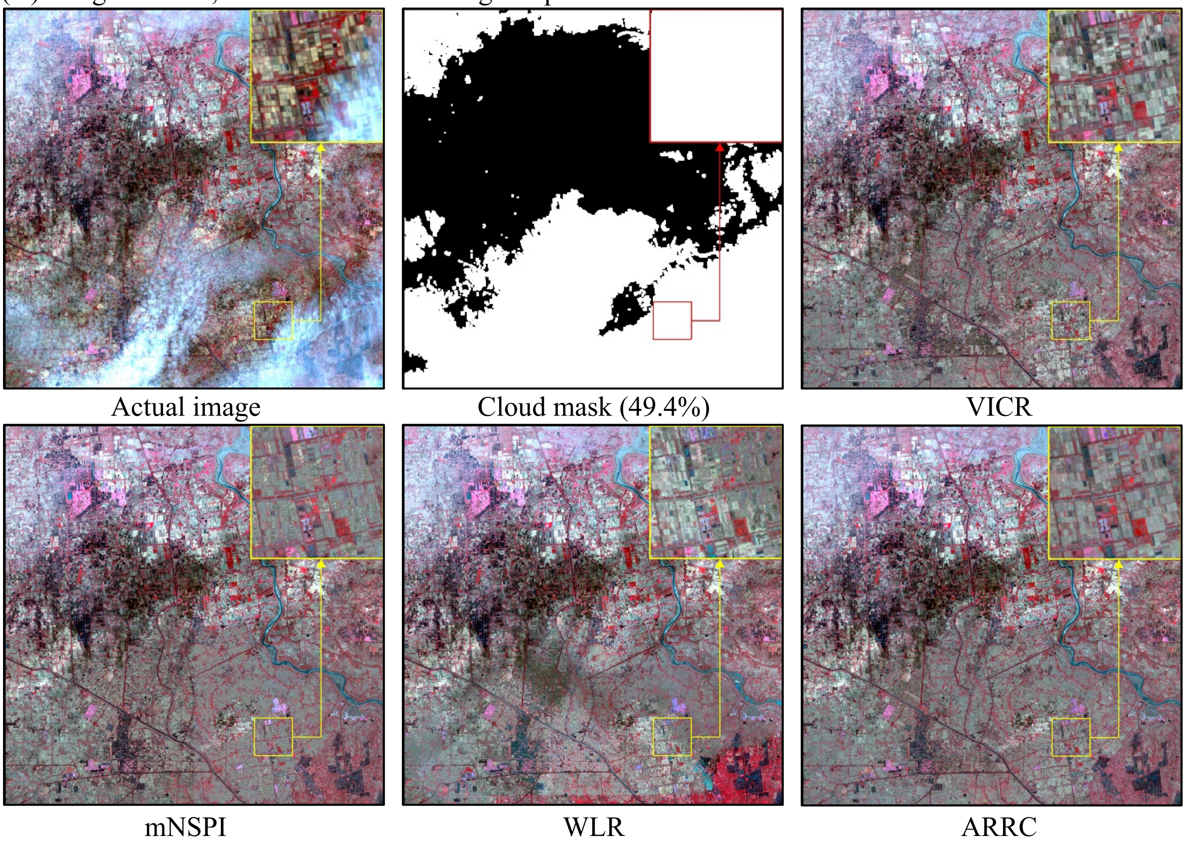

(B) Lower Gwydir Catchment, Landsat 5 TM SR image acquired on 03/18/05

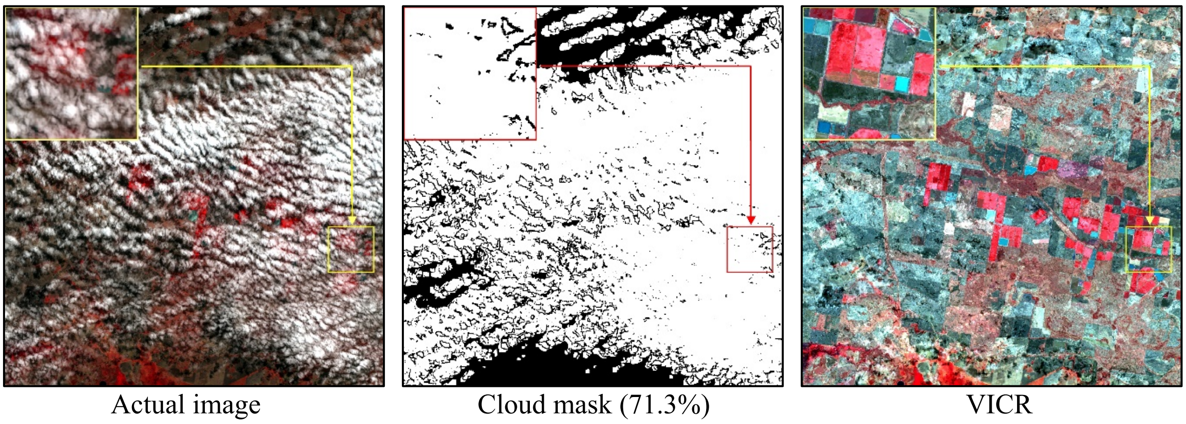

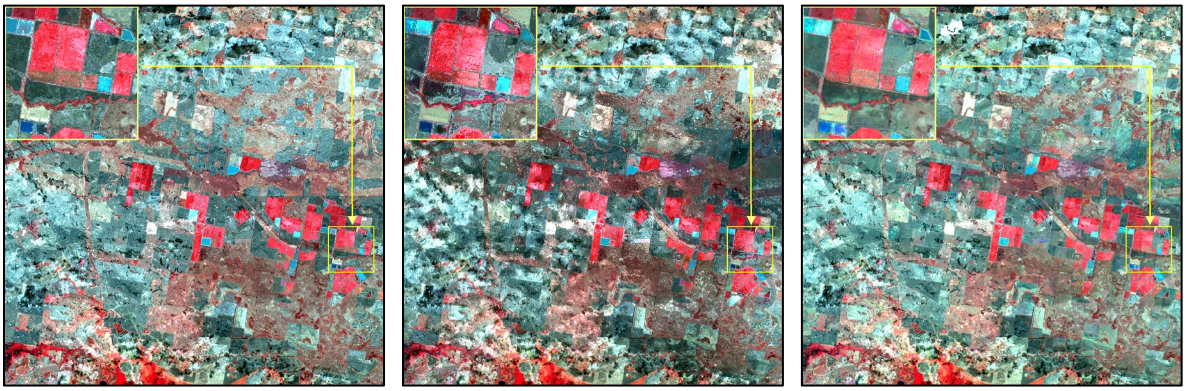

mNSPI WLR ARRC

(C) Beijing, Sensor: Landsat 8 OLI SR image acquired on 04/05/17

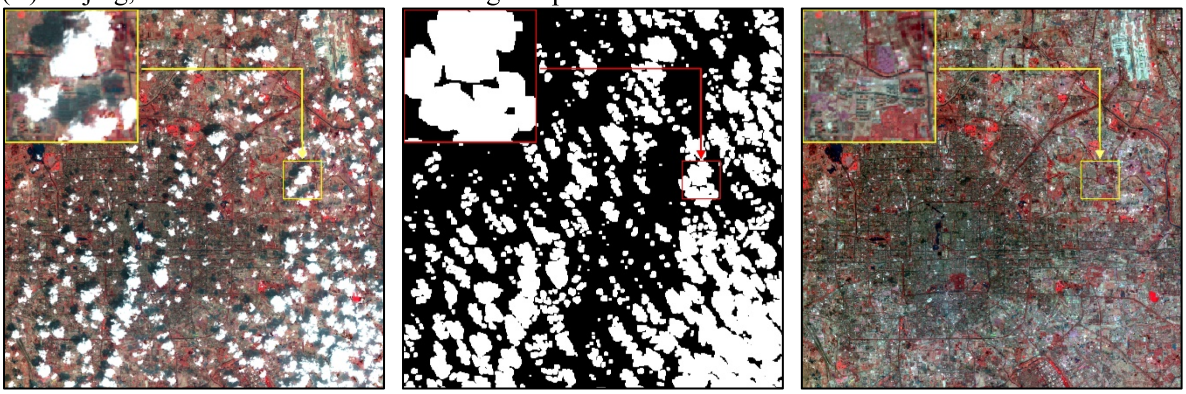

Actual image Cloud mask (35.1%) VICR

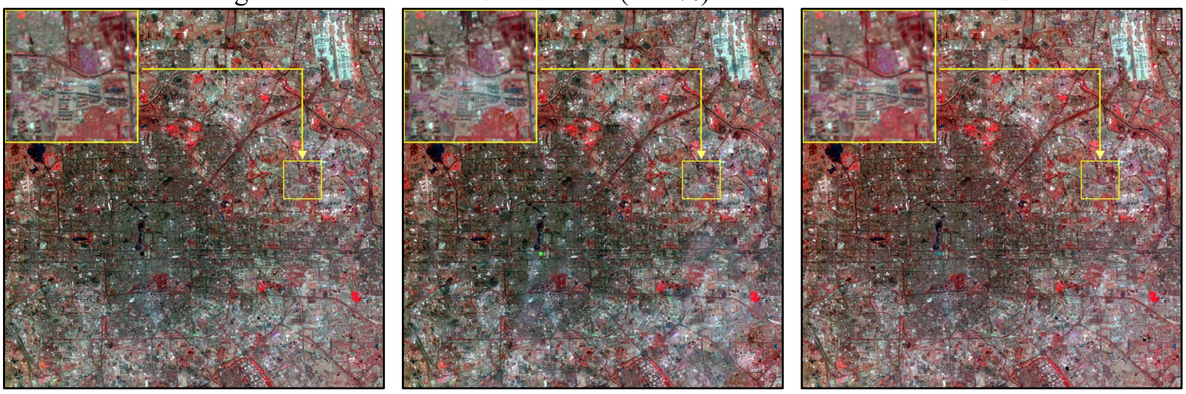

mNSPI WLR ARRC

(D) Yellow River Delta, Landsat 8 OLI SR image acquired on 07/18/19

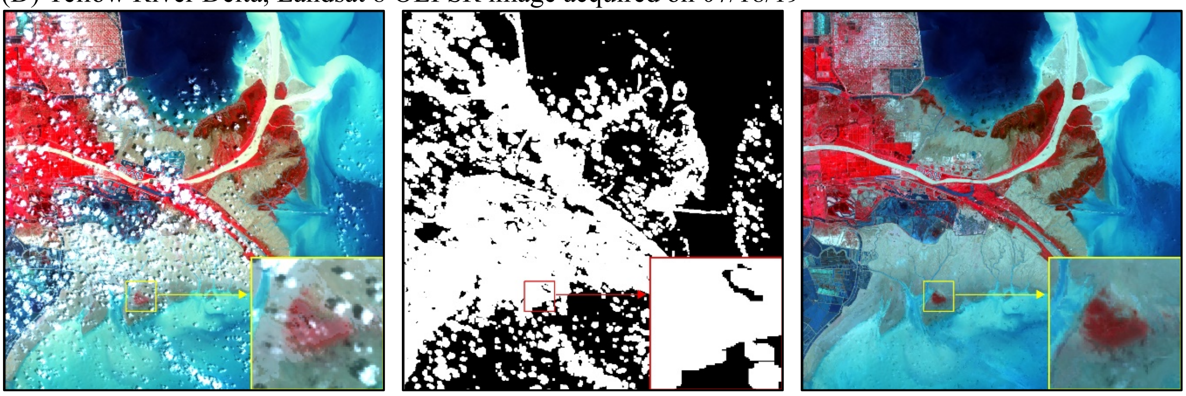

Actual image Cloud mask (41.8%) VICR

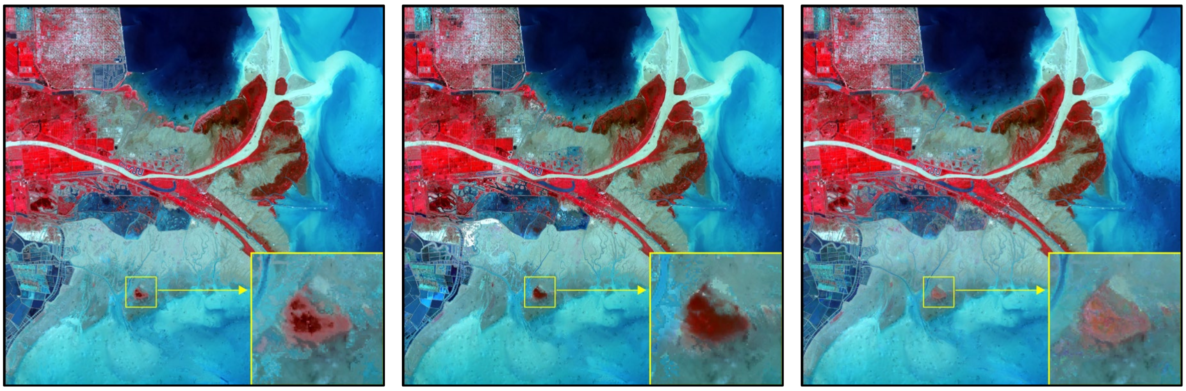

Fig. 13. Visual effects of reconstructed images from VICR, mNSPI, WLR and ARRC on real cloud-contaminated images over (A) Jianghan Plain, (B) Lower Gywdir Catchment, (C) Beijing and (D) Yellow River Delta.

Fig. 14 shows that the time series images recovered by VICR effectively supplemented the number of NDVI observations. The number of observations increased from 31 to 47 during 2015-2019 at the pixel in Jianghan Plain. The NDVI time series presented phenological dynamics well at both sites. In Jianghan Plain, rapeseed was normally harvested around May and then rice was planted. The crop rotation is observed in MOD13Q1 time series as it shows a local peak around March and a higher local peak around August. The local peak around March 2016 is not observed from the original Landsat NDVI time series but is well captured by the cloud-removed image (Fig. 14a). Likewise, the growing peak of paddy rice in August 2018 was better captured by the cloud-removed images (Fig. 14a). For the *Phragmites australis* marsh wetland pixel in Yellow River Delta, the reconstructed NDVI time series demonstrates greater variations than MOD13Q1. Negative NDVIs are obtained during December to February because the wetland pixel is covered by water in leaf-off season. In addition, the reconstructed NDVI time series better demonstrates growing and senescence patterns of *Phragmites australis* compared to the original time-series NDVI (e.g., in 2019).

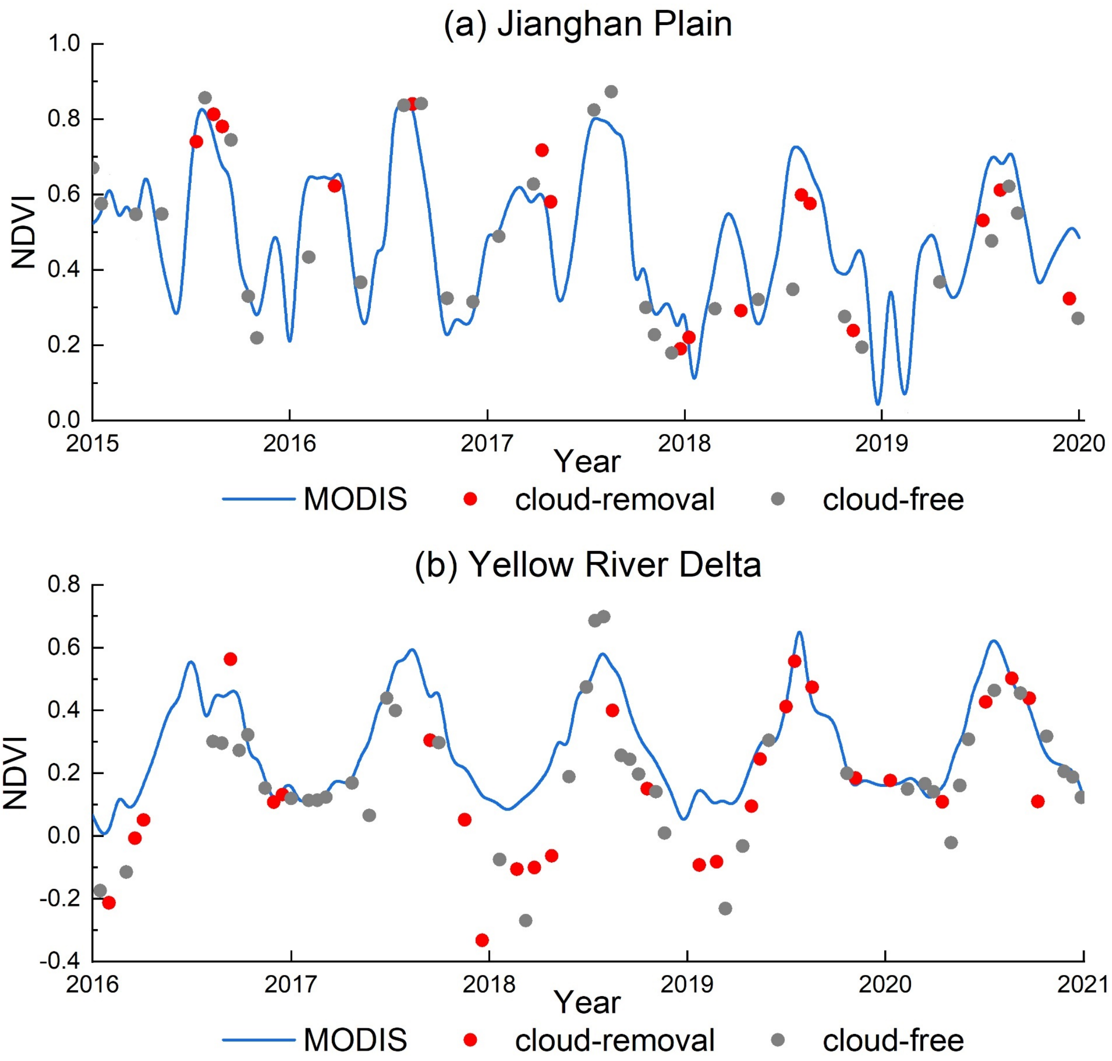

Fig. 14. NDVIs from cloud-free and cloud-removed Landsat images at (a) the pixel (30.2477°N, 112.8263°E) at a crop field in Jianghan Plain and (b) the pixel (37.8163°N, 119.0197°E) at *Phragmites australis* marsh wetland in Yellow River Delta. For comparison, MOD13Q1 NDVI time-series smoothed by spline function are plotted as blue line.

4.7 Experiment VII: Computation efficiency

We expect a good cloud removal algorithm to have reasonable computation efficiency besides high accuracy, so that it can be applied to large number of time-series images in an operational way. In this experiment, we compared the computing time of mNSPI, WLR, ARRC and VICR in Experiment III (the first sub-experiment) and Experiment V. We also calculated the total computing time of VICR for cloud removal from time-series Landsat images in Experiment VI. Although mNSPI is provided in IDL code and ARRC and VICR are written on MATLAB, previous comparisons showed equivalent efficiency between IDL and MATLAB (Liu et al., 2019).

Table 2 lists the computation time of mNSPI, WLR, ARRC and VICR when performing on the simulated cloud region in Experiment III. Fig. 15 illustrates the computation time averaged on each pixel in cloud regions with different sizes in Experiment V. In Experiment III, the computation time is: ARRC > mNSPI > VICR > WLR (Table 2). In most cases in Experiment V, the computation time per pixel of VICR is slightly longer than mNSPI and WLR. In both experiments, ARRC required much longer time than the other three methods. It is interesting that mNSPI took much longer time in Experiment III than in Experiment V even if the cloud sizes are similar. This is probably because mNSPI requires searching for the central pixel of the cloud region, and this process is much less efficient for irregular-shaped cloud than that for regular-shaped cloud. Therefore, it is expected that mNSPI has large variation in computation efficiency for reconstructing real cloud images. The total time of VICR for the largest cloud (160,000 pixels for 400×400 cloud) was only 480 seconds (maximum 0.003 seconds per pixel in Fig. 15). When processing time-series Landsat images in 5-year periods in Experiment VI, the cumulative processing time was around 15.4 hours (55,000 seconds) for Jianghan Plain (47 images) and 32.8 hours for Yellow River Delta (72 images) (Fig. S9).

Table 2. Elapsed time in seconds for different methods in Experiment III. The cloud pixels are 93312, 107529, 89813, and 103174 in Jianghan Plain, Lower Gwydir Catchment, Beijing and Yellow River Delta, respectively.

Testing sites	mNSPI	WLR	ARRC	VICR
Jianghan Plain	1892.44	40.89	3464.405	208.97
Lower Gwydir Catchment	1157.27	79.19	5923.87	347.70
Beijing	2407.62	49.14	3305.695	206.21
Yellow River Delta	1615.19	99.49	3883.475	215.64

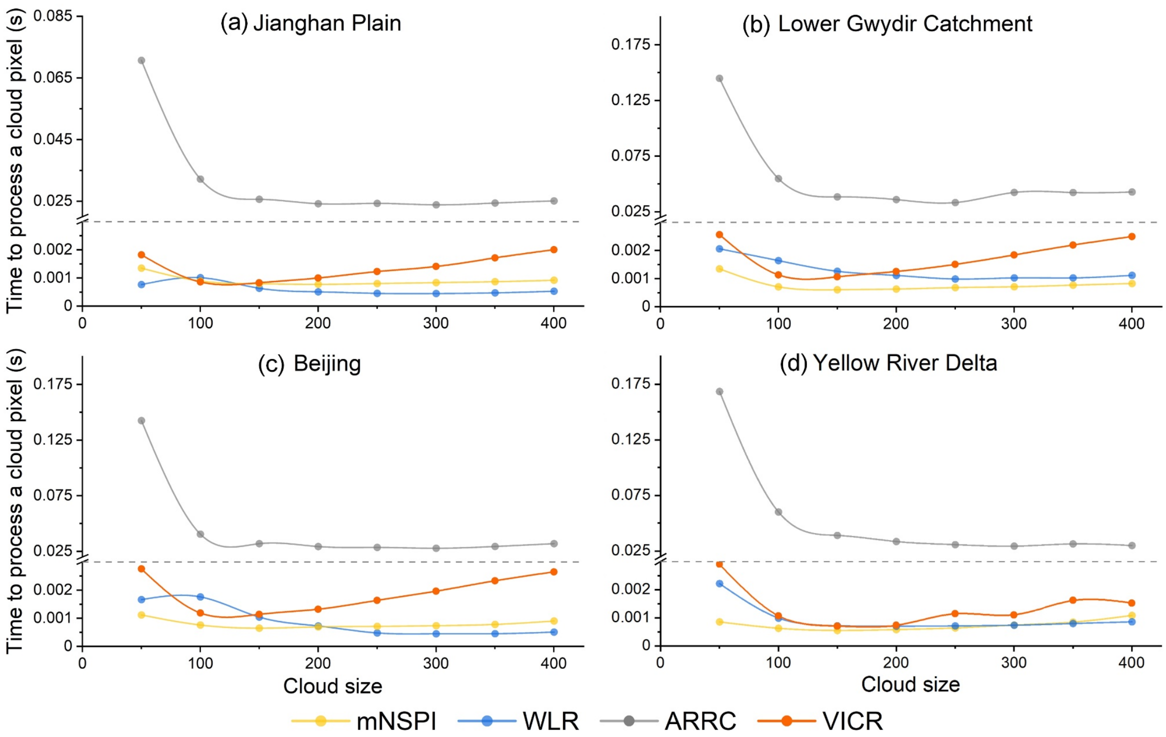

Fig. 15. Elapsed time per cloud pixel (in seconds) for mNSPI, WLR, ARRC and VICR for cloud size of 50×50, 100×100, 150×150, 250×250, 300×300, 350×350 and 400×400 pixels in Experiment V.

5. Discussion

VICR is different from previous algorithms in that it is based on virtual image construction. It is composed of patch-based virtual image prediction based on time-series reference images and pixel-based residual allocation incorporating spectral, temporal and spatial information.

Advantages of this algorithm are discussed in Section 5.1-5.3. The uncertainties of VICR are discussed in Section 5.4.

5.1 Virtual image construction for optimal reference images selection

The first improvement of VICR is that it allows automatic selection of optimal set of reference images. It is widely recognized that the selection of reference image has great impacts on the performance of cloud removal. Generally, the temporally closer reference image has more similar spectral characteristics to the target image so that higher reconstruction accuracy can be achieved (Zhu et al., 2012; Wang et al., 2021a). However, this might not be true when sudden land change occurred. In the coastal wetlands in Yellow River Delta, the closest reference image resulted in lower accuracies of mNSPI, WLR and ARRC than using reference image with longer time interval to the target image. Several approaches have been proposed to address this issue. Some studies considered using CC or SSIM to select the most similar reference image (Lin et al., 2013; Kalkan and Maktav, 2018), but it was also proved that this method did not improve the reconstruction accuracy considerably (Cao et al., 2020). STWR algorithm sorted the reference image patches based on the spectral similarity and selected the most similar three patches as reference images (Chen et al., 2017). It is hard to determine whether the three selected images can achieve the highest accuracy. Another solution is to incorporate long-term time-series reference images such as the ARRC long-term component. However, the ARRC long-term component is advantageous in capturing gradual temporal patterns of a pixel rather than capturing abrupt change (Cao et al., 2020). Our algorithm balances between ARRC and those algorithms depending on a fixed number of reference images because it can flexibly select the optimal set of reference images by virtual image construction strategy. In virtual image construction, the coefficient a_t represents the contribution of the reference image patch to the target image. As shown in Fig. S10, when the second reference image was added for Lower Gwydir Catchment and Yellow River Delta, the a_t value of the first reference image has a substantial decrease and becomes lower than that of the second image, indicating the second reference image has greater contribution in prediction. The varying a_t values when adding input reference images ensure that the land change pattern can be captured.

The idea of virtual image refers to the virtual image pair-based spatio-temporal fusion (VIPSTF) algorithm proposed by Wang et al. (2020), which constructs virtual Landsat-MODIS image pairs to predict image with the same spatial resolution as Landsat and the same temporal resolution as MODIS. The virtual image pair was generated by transplanting the linear relationship between time-series MODIS images to Landsat images. It was demonstrated theoretically that the virtual image pair is closer to the data at the prediction time than the known Landsat-MODIS image pairs (Wang et al., 2020). Inspired by this concept, in this study we constructed virtual image patch within cloud region to provide an initial prediction of the cloud image. We innovatively proposed to build two buffer zones around the cloud region, with each playing different roles. *Buf1* helps to establish linear relationship between time-series reference images and the target image, and *buf2* helps to find the optimal set of reference images. Results in Experiment I verified that this strategy is reasonable, and the results are reliable. More importantly, it eliminates the need for human intervention of reference image selection, which makes the algorithm more operational.

5.2 Advantages of TWSD and its potential applications

The second improvement of VICR is that the newly proposed TWSD can reduce the reconstruction errors by incorporating temporal information in similar pixel selection and residual allocation compared to the widely used *SD* (as illustrated in Section 4.2). The major contribution of TWSD to the accuracy improvement is in the process of similar pixel selection. Most existing similar-pixel selection methods assume that the similar pixels on the reference image remain similar on the cloud image (Chen et al., 2011), which is probably not true when land cover experienced abrupt change. For those methods based on multi-temporal or time-series reference images (such as ARRC), similar pixels are defined as those with similar temporal trend of spectral reflectance (Chen et al., 2016; Cao et al., 2020; Yan et al., 2018; Yan et al., 2020; Chen et al., 2021). The similarity metrics treats the multi-temporal (or time-series) reference images as equally important. However, in real cases, the greater the differences between the reference images and the cloud image, the reliability of the selected similar pixels based on these reference images will inevitably decrease. In this study, we developed TWSD by using the coefficient a_t obtained from linear regression model as the weight to consider different contributions from the reference images. A larger a_t value represents that the reference image at the corresponding time *t* contributes more to the prediction of the cloud image. This indicates that the similar pixels calculated based on this reference image are more reliable. A smaller a_t indicates that the similar pixel selected based on this reference image is less relevant.

TWSD has potential to be applied to other tasks requiring similar pixel selection such as spatial-temporal fusion (STF) algorithms, where spectral change in coarse resolution pixels need to be interpolated according to similarity between neighboring pixels and target pixels to reconstruct fine-resolution image (Zhu et al., 2018; Liu et al., 2019; Zhou et al., 2021). Some STF algorithms utilized multi-temporal Landsat-MODIS image pairs as references. Typical examples include ESTARFM (Enhanced Spatial and Temporal Adaptive Reflectance Fusion Model) (Zhu et al., 2010), STAIR (SaTellite dAta IntegRation) (Luo et al., 2018), and VIPSTF (Virtual image pairs-based spatio-temporal fusion) (Wang et al., 2020). In these algorithms, TWSD has potential be applied to calculate the spectral similarity in temporal domain in order to better select similar pixels and capture land change.

5.3 Robustness and efficiency of VICR method

Experiment III showed that VICR achieved better accuracies than mNSPI, WLR and ARRC, and the improvement in the accuracies was more obvious in the cases with abrupt land cover change. Compared to the other three algorithms, the performances of VICR were less affected when removing the closest reference image (Experiment IV) and were less affected with varying cloud sizes (Experiment V). This is understandable because VICR is not dependent on one reference image, and it flexibly selects the optimal set of time-series reference images. In addition, it captures temporal change in the key processes including virtual image construction, similar pixel selection and residual distribution by taking account temporal contribution of each reference image.

The results of Experiment VI and VII showed that VICR achieved good visual effects for real cloud removal and obtained reasonable time-series NDVI. It costs much less processing time than ARRC, and the cumulative processing time of cloud removal for five-year Landsat time-series images is acceptable. The good computational efficiency can be explained by that the linear regression for virtual image construction is conducted based on image patches instead of individual pixels. Different from ARRC that performs autoregression for all neighboring pixels and calculates the contribution of all neighboring pixels to the target pixel, the virtual image construction based on image patches can substantially improve the computation efficiency. The combination of patch-based virtual image construction and pixel-based residual distribution enables both good accuracy and efficiency. The promising performance and high computing efficiency highlighted the operationality of VICR for cloud removal from a large volume of Landsat datasets.

5.4 Uncertainties and implications for future research

In practical applications of VICR, there are some factors that lead to uncertainties in the cloud removal results. First, VICR still requires reference images to be cloud free within a cloud region. When the cloud region is too large, it may be difficult to select sufficient reference images. This problem can be addressed by time-series cloud removal strategy in Experiment VI. The images with low cloud cover are given higher priority for cloud removal, and these reconstructed images can be used as reference images to remove large cloud. One concern is that the errors produced in the images with small cloud cover may magnify the errors for cloud removal in the image with large cloud. To address this concern, we further conducted an experiment. We simulated a large cloud on the target images in Table 1. The shape of the cloud was taken from the real images in Fig. 13 for each site. We removed the cloud following the same procedure in Experiment III using VICR (we call single image reconstruction). We also put the cloud-simulated image into the time-series Landsat images and reconstruct each image in order of the cloud cover percentage (same as time-series cloud removal procedure in Experiment VI). The time-series Landsat images are listed in Table S1 and the reconstructed images are shown in Figure S11. Fig. 16 shows that the RMSEs of the reconstructed images from the time-series cloud removal procedure are comparable or even lower than those from the single image reconstruction. This is because the cloud-removed images provide better temporally closer information for reconstruction of the image with larger cloud cover. Nonetheless, both results show acceptable RMSEs and good visual effects (Figure S11), indicating the time-series cloud removal strategy is suitable in the extreme cases where satisfactory reference images are hard to be found for the large cloud region.

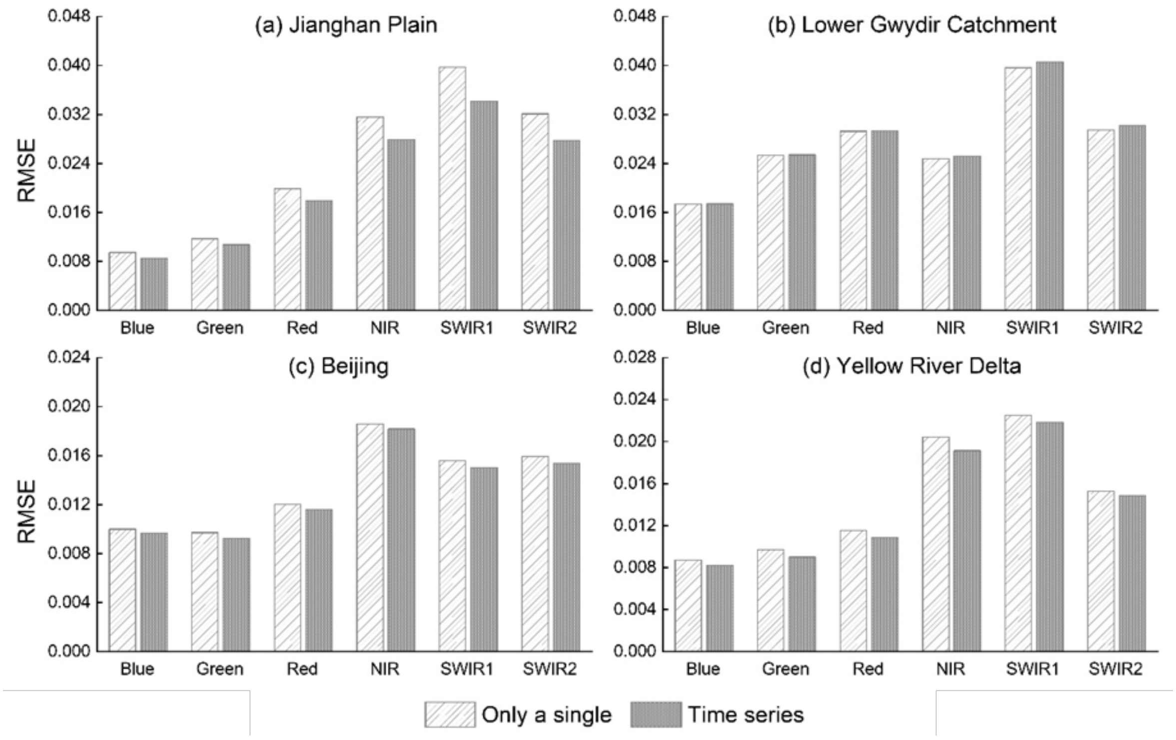

Fig. 16. RMSEs of the reconstructed images from VICR for single image cloud removal procedure and time-series image cloud removal procedure at Jianghan Plain, Lower Gwydir Catchment, Beijing and Yellow River Delta.

Second, in this study we only tested VICR on an identical Landsat sensor. Therefore, the shortest time interval from the reference image to the target image was 16 days. We didn't incorporate Landsat ETM+ images mainly because the ETM+ sensor had missing strips owing to the failure of the scan-line corrector after May 2003. As Landsat 9 OLI-2 sensor has similar spectral characteristics as Landsat 8 OLI and provides images with 8-day offset with Landsat 8, the performances of VICR for cloud removal have great potential for enhancement when images from both sensors are included. In addition, future work may consider incorporating Harmonized Landsat-8 Sentinel-2 surface reflectance (Claverie et al., 2018) to generate time-series cloud-free images with high temporal frequency.

6. Conclusion

This paper proposed a new thick cloud removal algorithm (VICR) for Landsat images based on the concept of virtual image. The optimal set of reference images is determined automatically by establishing two buffer zones around the cloud region. Similar pixels are selected based on the newly proposed TWSD and used to estimate residual image in the cloud region. Seven experiments were performed at four sites representing different landscape patterns and land change dynamics, and the proposed VICR was compared to existing mNSPI, WLR and ARRC algorithms. The main findings are summarized as follows:

1) VICR achieved better reconstruction accuracies than mNSPI, WLR and ARRC. Results on the cloud-simulated images showed that VICR yielded higher CC, lower RMSE and higher SSIM than mNSPI and WLR (e.g., RMSEs of VICR vs. MNSPI: 0.0288 vs. 0.0405, 0.0286 vs. 0.0382, 0.0193 vs. 0.0227, 0.0234 vs. 0.0317 in the NIR bands for four sites, respectively). VICR yielded higher CC and lower RMSE than ARRC and in most cases yielded higher SSIM than ARRC (e.g., RMSE of VICR vs. ARRC: 0.0193 vs. 0.0211, 0.0286 vs. 0.0302 and SSIM of VICR vs. ARRC: 0.9374 vs. 0.9375, 0.8860 vs. 0.8898 in the NIR bands for Beijing and Lower Gwydir Catchment, respectively). Experiments on both cloud-simulated

image and real cloud-contaminated images showed that VICR generated visually better reconstruction results than the other algorithms. The accuracy improvement was especially obvious for the sites with abrupt land change, i.e., Lower Gwydir Catchment and Yellow River Delta.

2) VICR is more robust than mNSPI, WLR and ARRC in terms of the sensitivities to reference image and different cloud sizes. When removing the temporally closest reference image, VICR still achieved the lowest RMSEs (e.g., RMSE: 0.0321, 0.0309, 0.0266 and 0.02496 at NIR band for the four sites). The RMSEs of VICR were less affected especially for the Yellow River Delta with surface reflectance change induced by tidal inundation. In addition, VICR shows smaller fluctuations in RMSEs with increasing cloud size from 50×50 to 400×400 pixels.

3) VICR requires much less computation time than ARRC, and less computation time than mNSPI for irregular-shaped clouds. The processing time for cloud removal in 5-year Landsat images was reasonable (e.g., 32.8 hours in Yellow River Delta).

4) The major advantages of VICR are that it allows automatics determination of optimal set of time-series reference images, and it better incorporates temporal change information. The robustness and efficiency of VICR can promote its operational use in large datasets processing.

Credit author statement

Zhanpeng Wang: Methodology, Investigation, Data processing, Software, Writing-Original Draft. Yinghai Ke: Conceptualization, Methodology, Investigation, Financial acquisition, Writing - Original Draft, Writing-Review & Editing. Demin Zhou: Supervision, Financial acquisition. Xiaojuan Li: Investigation, Project administration. Huili Gong: Investigation, Project administration.

Declaration of Competing Interest

The authors declare that they have no known competing financial interests or personal relationships that could have appeared to influence the work reported in this paper.

Acknowledgments

The work is supported by the National Natural Science Foundation of China [grant number 42071396]; and Beijing Science and Technology Planning Project [grant number Z201100006720001].

References

Cao, R.Y., Chen, Y., Chen, J., et al., 2020. Thick cloud removal in Landsat images based on autoregression of Landsat time-series data. *Remote Sensing of Environment, 249.*

Chen, B., Chen, L., Huang, B., et al., 2018. Dynamic monitoring of the Poyang Lake wetland by integrating Landsat and MODIS observations. *ISPRS Journal of Photogrammetry and Remote Sensing, 139*, 75-87.

Chen, B., Huang, B., Chen, L., et al., 2017. Spatially and Temporally Weighted Regression: A Novel Method to Produce Continuous Cloud-Free Landsat Imagery. *IEEE Transactions on Geoscience and Remote Sensing, 55*, 27-37.

Chen, J., Zhu, X., Vogelmann, J.E., et al., 2011. A simple and effective method for filling gaps in Landsat ETM+ SLC-off images. *Remote Sensing of Environment, 115*, 1053-1064.

Chen, Y., Cao, R., Chen, J.,et al., 2021. A practical approach to reconstruct high-quality Landsat

NDVI time-series data by gap filling and the Savitzky–Golay filter. *ISPRS Journal of Photogrammetry and Remote Sensing,* 180, 174-190

Cheng, Q., Shen, H., Zhang, L., et al., 2014. Cloud removal for remotely sensed images by similar pixel replacement guided with a spatio-temporal MRF model. *ISPRS Journal of Photogrammetry and Remote Sensing, 92*, 54-68.

Claverie, M., Ju, J., Masek, J.G., et al., 2018. The Harmonized Landsat and Sentinel-2 surface reflectance data set. *Remote Sensing of Environment, 219*, 145-161.

Du, W., Qin, Z., Fan, J., Gao., et al., 2019. An Efficient Approach to Remove Thick Cloud in VNIR Bands of Multi-Temporal Remote Sensing Images. *Remote Sensing, 11.*

Fang, Y., Ren, T., Zhang, S., et al., 2021. Rotation with oilseed rape as the winter crop enhances rice yield and improves soil indigenous nutrient supply. *Soil and Tillage Research, 212*, 105065

Gao, J., Yi, Y., Wei, T., et al., 2021. Sentinel-2 Cloud Removal Considering Ground Changes by Fusing Multitemporal SAR and Optical Images. *Remote Sensing, 13.*

Huang, Z., Liu, X., Yang, Q., et al., 2021. Quantifying the spatiotemporal characteristics of multi-dimensional karst ecosystem stability with Landsat time series in southwest China. *International Journal of Applied Earth Observation and Geoinformation, 104*, 102575.

Kalkan, K.,Maktav, M.D., 2018. A Cloud Removal Algorithm to Generate Cloud and Cloud Shadow Free Images Using Information Cloning. *Journal of the Indian Society of Remote Sensing, 46*, 1255-1264.

Kokhanovsky, A.A., 2013. Remote sensing of atmospheric aerosol using spaceborne optical observations. *Earth-Science Reviews, 116*, 95-108.

Li, L., Shi, R., Zhang, L., et al., 2014. The data fusion of aerosol optical thickness using universal kriging and stepwise regression in East China. In, *Remote Sensing and Modeling of Ecosystems for Sustainability XI* (p. 922112): International Society for Optics and Photonics

Li, Q., Cui, J., Jiang, W., et al., 2021. Monitoring of the Fire in Muli County on March 28, 2020, based on high temporal-spatial resolution remote sensing techniques. *Natural Hazards Research, 1*, 20-31.

Li, X., Wang, L., Cheng, Q., et al., 2019. Cloud removal in remote sensing images using nonnegative matrix factorization and error correction. *ISPRS Journal of Photogrammetry and Remote Sensing, 148*, 103-113.

Lin, C.H., Tsai, P.H., Lai, K.H., et al., 2013. Cloud Removal From Multitemporal Satellite Images Using Information Cloning. *IEEE Transactions on Geoscience and Remote Sensing, 51*, 232-241.

Liu, M.L, Ke, Y.H., Qi, Y., et al., 2019. Comparison of Five Spatio-Temporal Satellite Image Fusion Models over Landscapes with Various Spatial Heterogeneity and Temporal Variation. *Remote Sensing, 11*.

Luo, Y., Guan, K., Peng, J., 2018. STAIR: A generic and fully-automated method to fuse multiple sources of optical satellite data to generate a high-resolution, daily and cloud-/gap-free surface reflectance product. *Remote Sensing of Environment, 214*, 87-99.

Malek, S., Melgani, F., Bazi, Y., et al., 2018. Reconstructing Cloud-Contaminated Multispectral Images With Contextualized Autoencoder Neural Networks. *IEEE Transactions on Geoscience and Remote Sensing, 56*, 2270-2282

Meraner, A., Ebel, P., Zhu, X.X., et al., 2020. Cloud removal in Sentinel-2 imagery using a deep residual neural network and SAR-optical data fusion. *ISPRS J Photogramm Remote Sens, 166*, 333-346.

Nijland, W., Reshitnyk, L.,Rubidge, E., 2019. Satellite remote sensing of canopy-forming kelp on a complex coastline: A novel procedure using the Landsat image archive. *Remote Sensing of Environment, 220*, 41-50.

Shen, H., Li, X., Cheng, Q., et al., 2015. Missing Information Reconstruction of Remote Sensing Data: A Technical Review. *IEEE Geoscience and Remote Sensing Magazine, 3*, 61-85.

Shen, H., Wu, J., Cheng, Q., et al., 2019. A Spatiotemporal Fusion Based Cloud Removal Method for Remote Sensing Images With Land Cover Changes. *IEEE Journal of Selected Topics in Applied Earth Observations and Remote Sensing, 12*, 862-874.

Shi, Y., Burns, M., Ritchie, R.J., et al., 2014. Probabilistic risk assessment of diuron and prometryn in the Gwydir River catchment, Australia, with the input of a novel bioassay based on algal growth. *Ecotoxicology and Environmental Safety, 106*, 213-219.

Siravenha, A.C., Sousa, D., Bispo, A., et al., 2011. Evaluating inpainting methods to the satellite images clouds and shadows removing. In, *International Conference on Signal Processing, Image Processing, and Pattern Recognition* (pp. 56-65): Springer.

Tao, J.B., Liu, W.B., Tan, W.X., et al., 2019. Fusing multi-source data to map spatio-temporal dynamics of winter rape on the Jianghan Plain and Dongting Lake Plain, China. *Journal of Integrative Agriculture, 18*, 2393-2407.

Vuolo, F., Ng, W.T., Atzberger, C., 2017. Smoothing and gap-filling of high resolution multi-spectral time series: Example of Landsat data. *International Journal of Applied Earth Observation and Geoinformation, 57*, 202-213

Wang, Q., Tang, Y., Tong, X., et al., 2020. Virtual image pair-based spatio-temporal fusion.

Remote Sensing of Environment, 249.

Wang, Q., Wang, L., Li, Z., et al., 2021a. Spatial–Spectral Radial Basis Function-Based Interpolation for Landsat ETM+ SLC-Off Image Gap Filling. *IEEE Transactions on Geoscience and Remote Sensing, 59*, 7901-7917.

Wang, Z., Ke, Y., Chen, M., et al., 2021b. Mapping coastal wetlands in the Yellow River Delta, China during 2008–2019: impacts of valid observations, harmonic regression, and critical months. *International Journal of Remote Sensing, 42*, 7880-7906.

Xu, H., Tang, X., Ai, B., et al., 2021. Missing data reconstruction in VHR images based on progressive structure prediction and texture generation. *ISPRS Journal of Photogrammetry and Remote Sensing, 171*, 266-277.

Xu, M., Deng, F., Jia, S., et al., 2022. Attention mechanism-based generative adversarial networks for cloud removal in Landsat images. *Remote Sensing of Environment, 271*.

Yan, L., & Roy, D., 2018. Large-Area Gap Filling of Landsat Reflectance Time Series by Spectral-Angle-Mapper Based Spatio-Temporal Similarity (SAMSTS). *Remote Sensing,* 10

Yan, L., & Roy, D.P., 2020. Spatially and temporally complete Landsat reflectance time series modelling: The fill-and-fit approach. *Remote Sensing of Environment,* 241, 111718

Zeng, C., Shen, H., Zhang, L., 2013. Recovering missing pixels for Landsat ETM+ SLC-off imagery using multi-temporal regression analysis and a regularization method. *Remote Sensing of Environment, 131*, 182-194.

Zhang, Q., Yuan, Q., Zeng, C., et al., 2018. Missing Data Reconstruction in Remote Sensing Image With a Unified Spatial–Temporal–Spectral Deep Convolutional Neural Network. *IEEE Transactions on Geoscience and Remote Sensing, 56*, 4274-4288.

Zhang, Q., Yuan, Q., Li, J., et al., 2020. Thick cloud and cloud shadow removal in multitemporal imagery using progressively spatio-temporal patch group deep learning. *ISPRS Journal of Photogrammetry and Remote Sensing, 162*, 148-160.

Zhang, Q., Yuan, Q., Li, Z., et al., 2021. Combined deep prior with low-rank tensor SVD for thick cloud removal in multitemporal images. *ISPRS Journal of Photogrammetry and Remote Sensing, 177*, 161-173.

Zheng, J., Liu, X.Y., Wang, X., 2021. Single Image Cloud Removal Using U-Net and Generative Adversarial Networks. *IEEE Transactions on Geoscience and Remote Sensing, 59*, 6371-6385.

Zhou, J., Chen, J., Chen, X., et al., 2021. Sensitivity of six typical spatiotemporal fusion methods to different influential factors: A comparative study for a normalized difference vegetation index time series reconstruction. *Remote Sensing of Environment, 252.*

Zhou, W., Bovik, A. C., Sheikh, H. R., et al. 2004. Image Qualifty Assessment: From Error Visibility to Structural Similarity. *IEEE Transactions Transactions on Image Processing.* 13(4), 600–612.

Zhu, X., Chen, J., Gao, F., et al., 2010. An enhanced spatial and temporal adaptive reflectance fusion model for complex heterogeneous regions. *Remote Sensing of Environment, 114*, 2610-2623.

Zhu, X., Cai, F., Tian, J., et al., 2018. Spatiotemporal Fusion of Multisource Remote Sensing Data: Literature Survey, Taxonomy, Principles, Applications, and Future Directions. *Remote Sensing*, 10.

Zhu, X., Gao, F., Liu, D., et al., 2012. A Modified Neighborhood Similar Pixel Interpolator

Approach for Removing Thick Clouds in Landsat Images. *IEEE Geoscience and Remote Sensing Letters, 9*, 521-525.

Zhu, Z., Zhang, J., Yang, Z., et al. 2020. Corrigendum to continuous monitoring of land disturbance based on Landsat time series. *Remote Sensing of Environment, 244*, 111824.

[Supplementary Materials for]

Virtual image patch-based cloud removal for Landsat images

Zhanpeng Wang[a], Yinghai Ke[a,b,c*], Demin Zhou[a,b,c], Xiaojuan Li[a,b,c], Lin Zhu[a,b,c], Huili Gong[a,b,c]

[a] College of Resource Environment and Tourism, Capital Normal University, Beijing, 100048, China

[b] Laboratory Cultivation Base of Environment Process and Digital Simulation, Capital Normal University, Beijing, 100048, China

[c] Beijing Laboratory of Water Resources Security, Capital Normal University, Beijing, China

Corresponding Author: Yinghai Ke, Ph. D, yke@cnu.edu.cn

Contents of this file

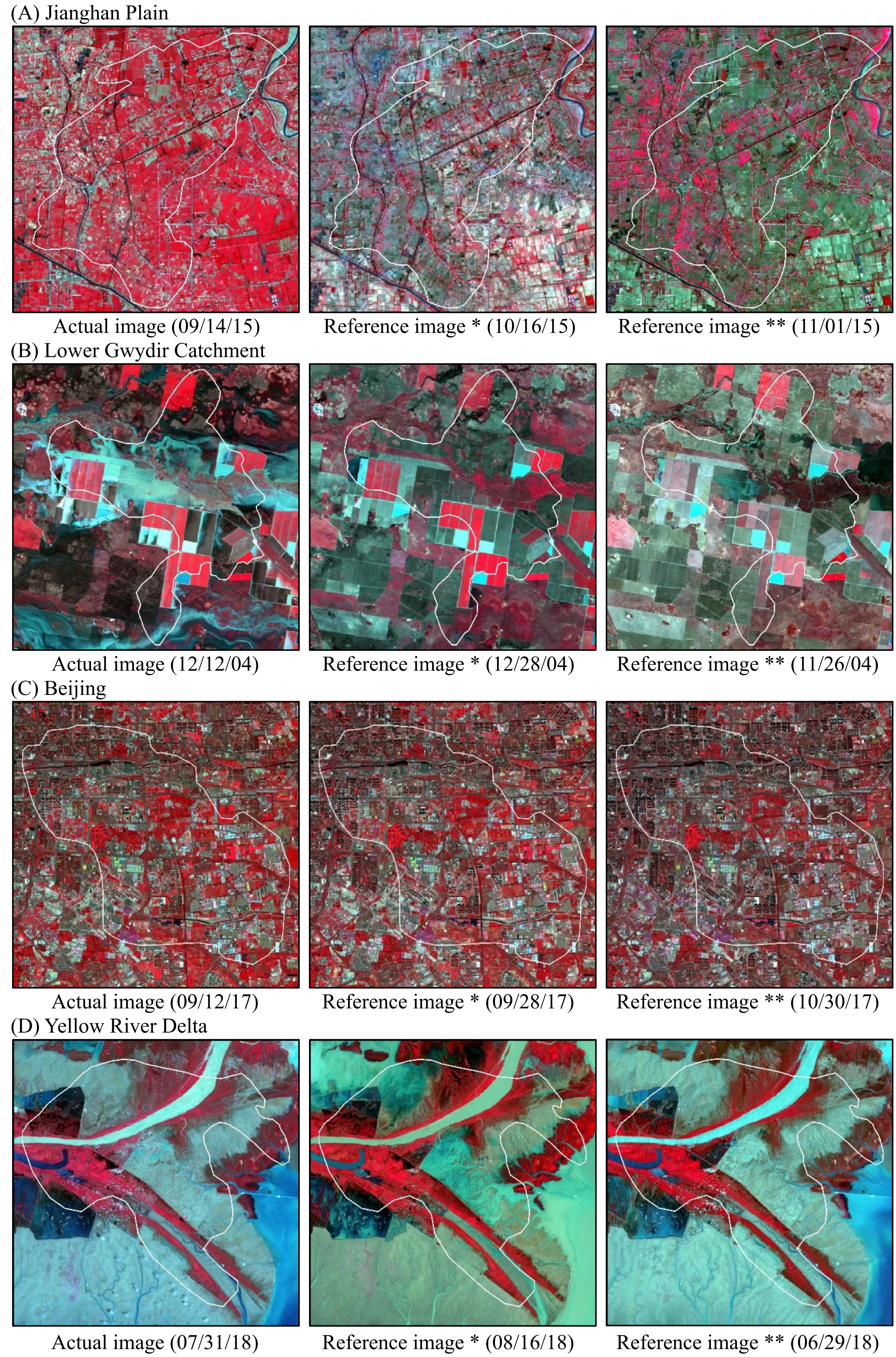

Fig. S1. The zoom-in actual image, reference image* and reference image** in the cloud region (polygon in white border) in standard false color composition in (A) Jianghan Plain, (B) Lower Gwydir Catchment, (C) Beijing and (D) Yellow River Delta.

(A) Jianghan Plain, Landsat 8 OLI SR image acquired on 12/16/14 (image composition with SWIR1, Red and Green)

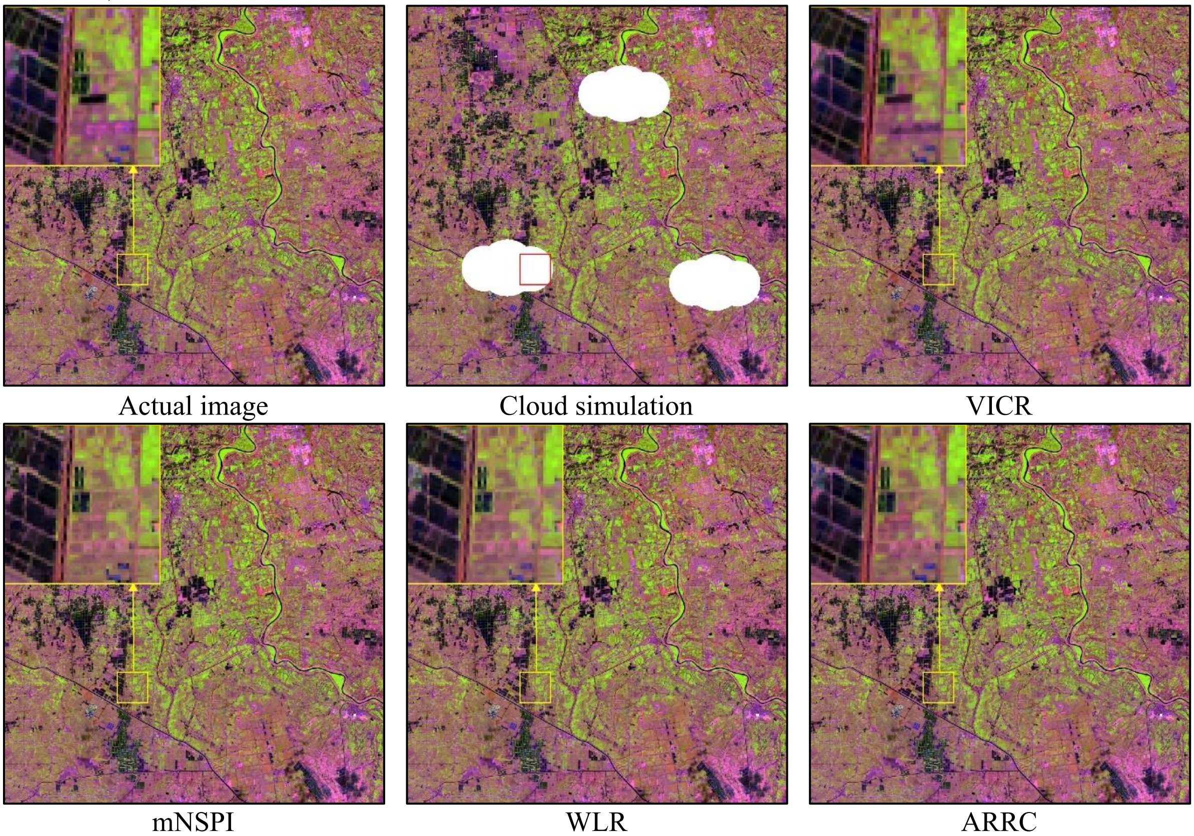

(B) Lower Gwydir Catchment, Landsat 5 TM SR image acquired on 12/12/04

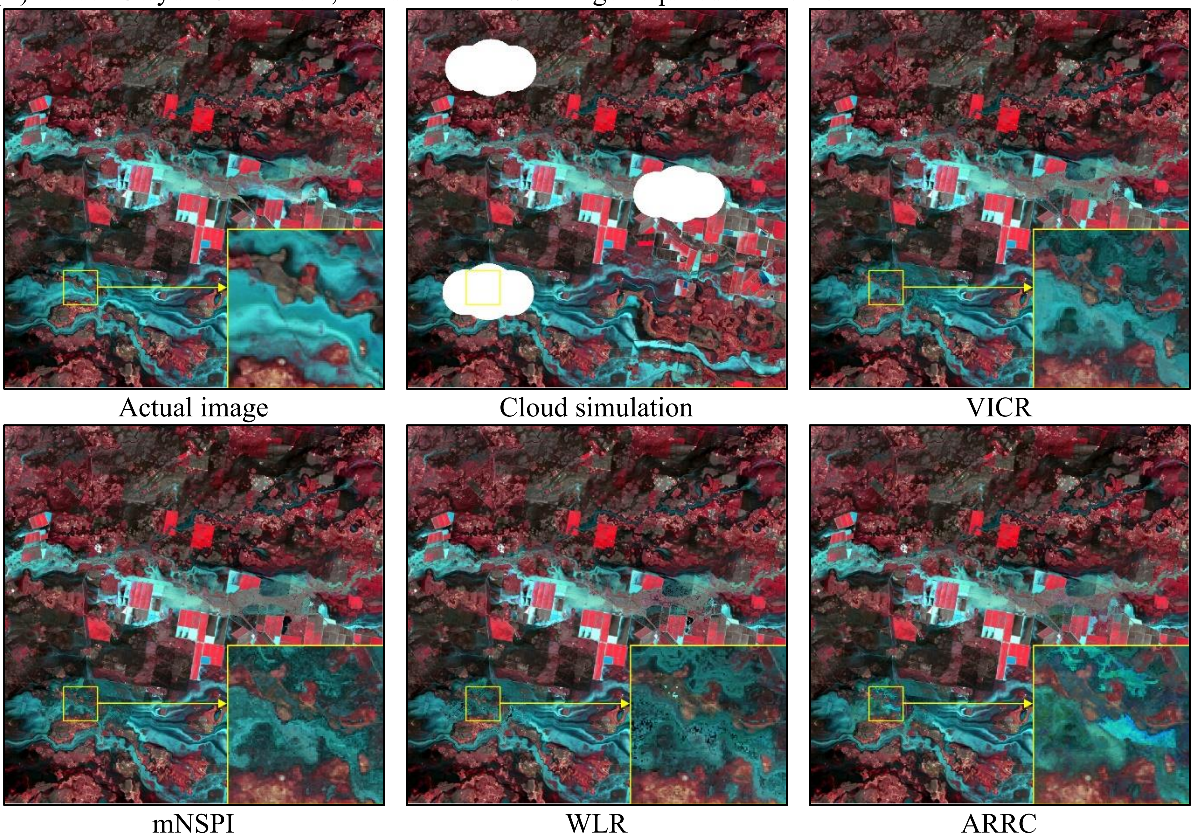

(C) Beijing, Landsat 8 OLI SR image acquired on 05/23/17

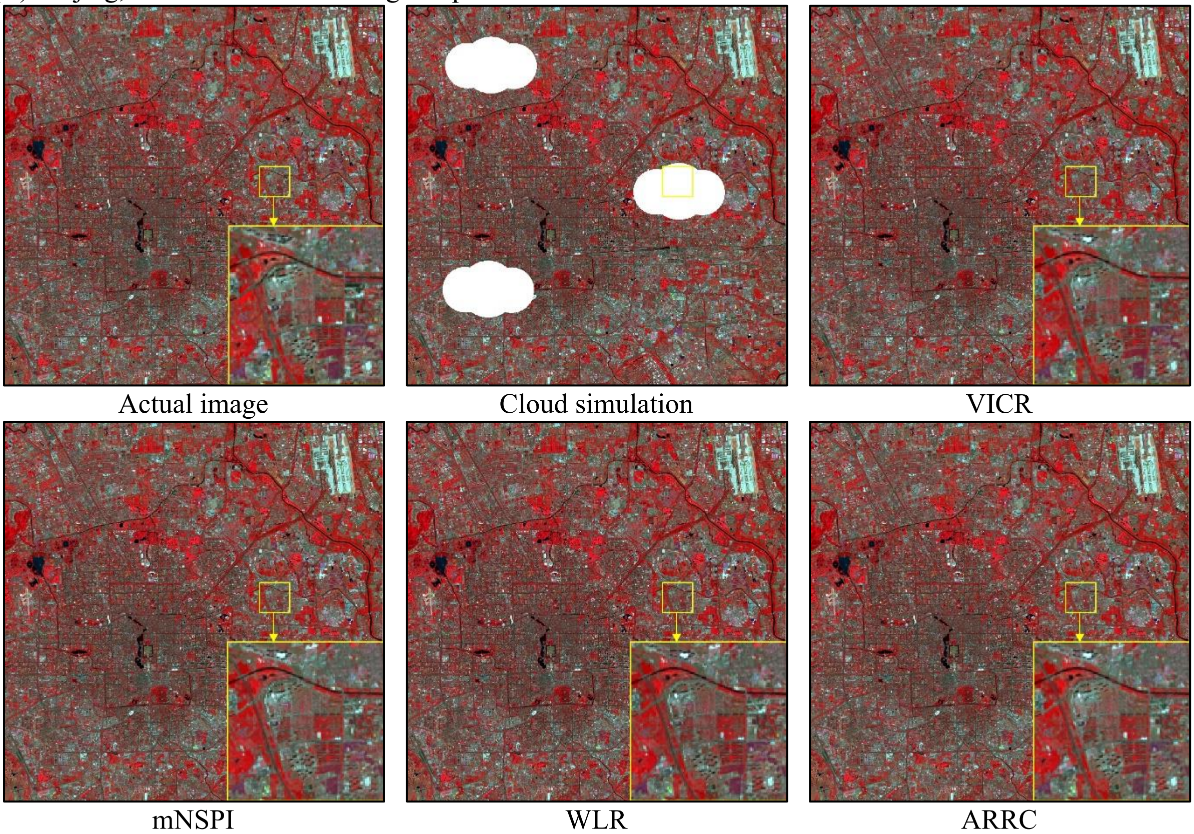

(D) Yellow River Delta, Landsat 8 OLI SR image acquired on 06/29/18

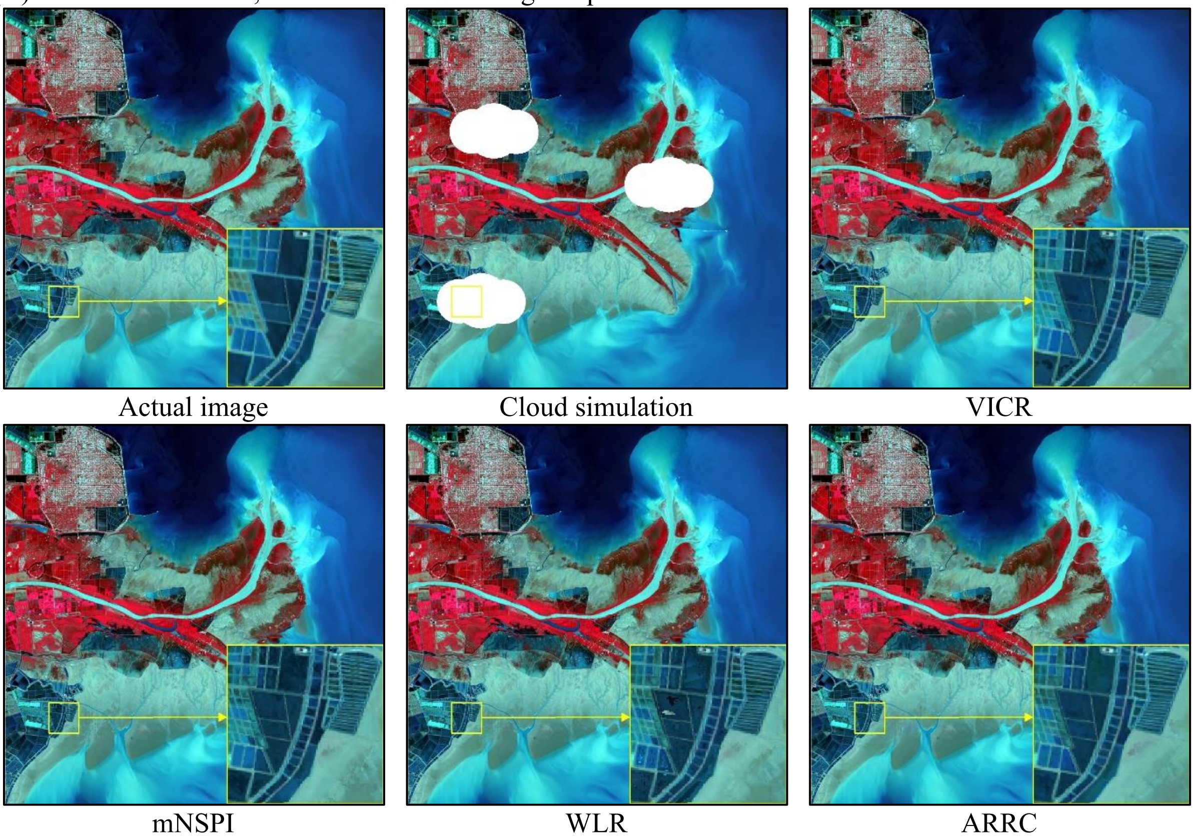

Fig. S2. Visual comparisons between mNSPI, WLR, ARRC, and VICR the multi-clouds simulation images over (A) Jianghan Plain, (B) Lower Gwydir Catchment, (C) Beijing and (D) Yellow River Delta. The reference images for mNSPI, WLR, ARRC short-term component are acquired on 11/14/14 for (A), 12/28/04 for (B), 05/07/17 for (C) and 07/31/18 for (D)

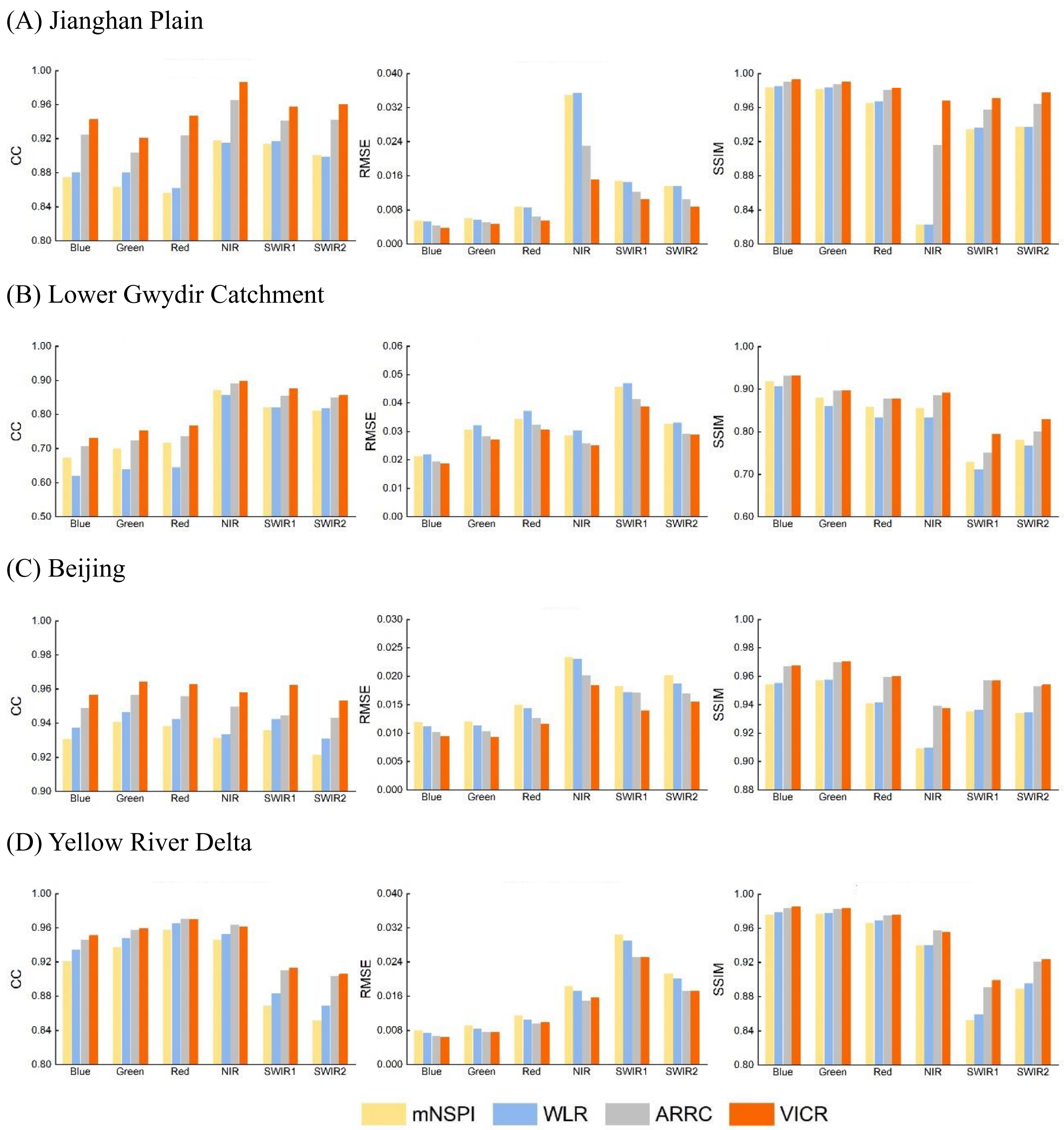

Fig. S3. Comparisons of CC (left column), RMSE (center column) and SSIM (right column) between mNSPI, WLR, ARRC, and VICR for the multi-clouds simulation images over (A) Jianghan Plain, (B) Lower Gwydir Catchment, (C) Beijing and (D) Yellow River Delta.

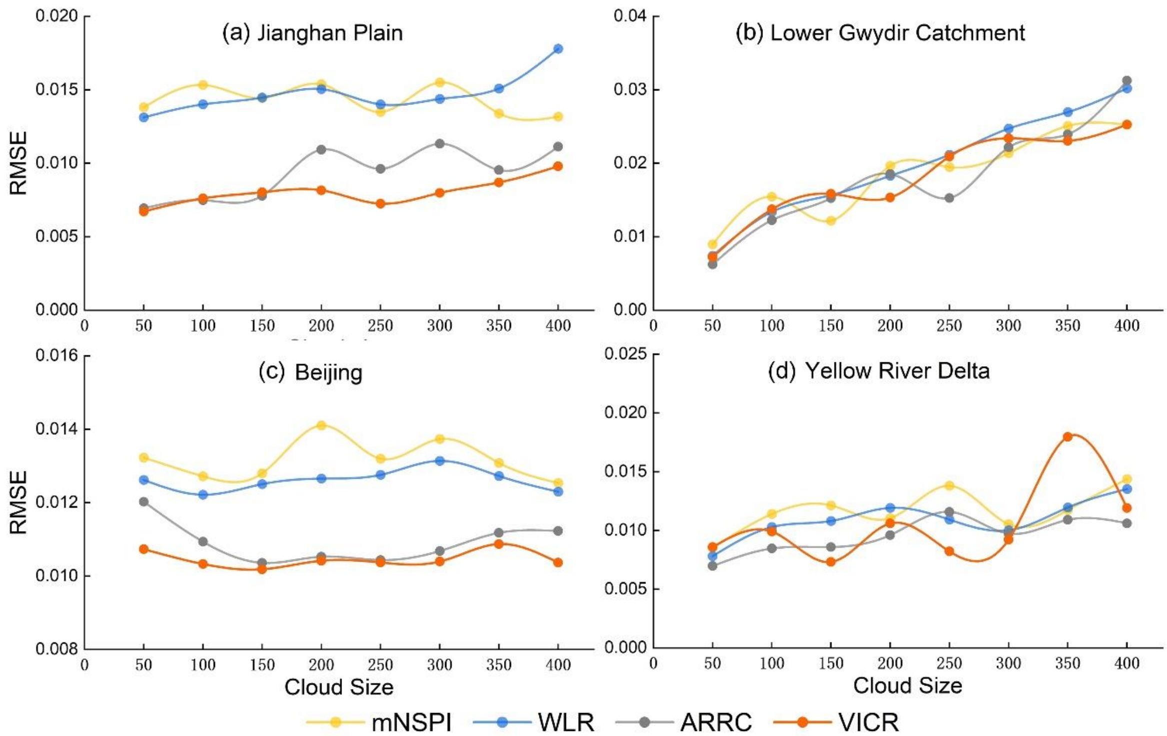

Fig. S4. The RMSEs of the reconstructed images from mNSPI, WLR, ARRC, and VICR at blue band for cloud sizes ranging from 50×50 pixels to 400×400 pixels. Note that the RMSEs were calculated for the 50×50 pixels in the center of the clouds.

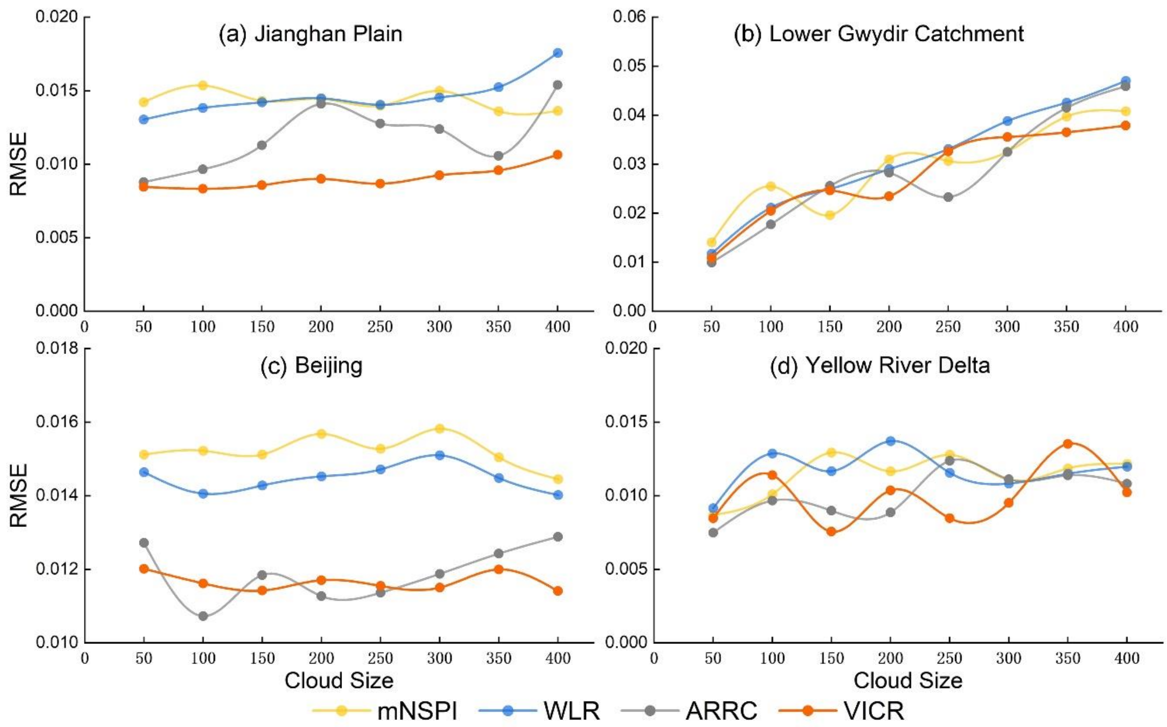

Fig. S5. The RMSEs of the reconstructed images from mNSPI, WLR, ARRC, and VICR at **green** band for cloud sizes ranging from 50×50 pixels to 400×400 pixels. Note that the RMSEs were calculated for the 50×50 pixels in the center of the clouds.

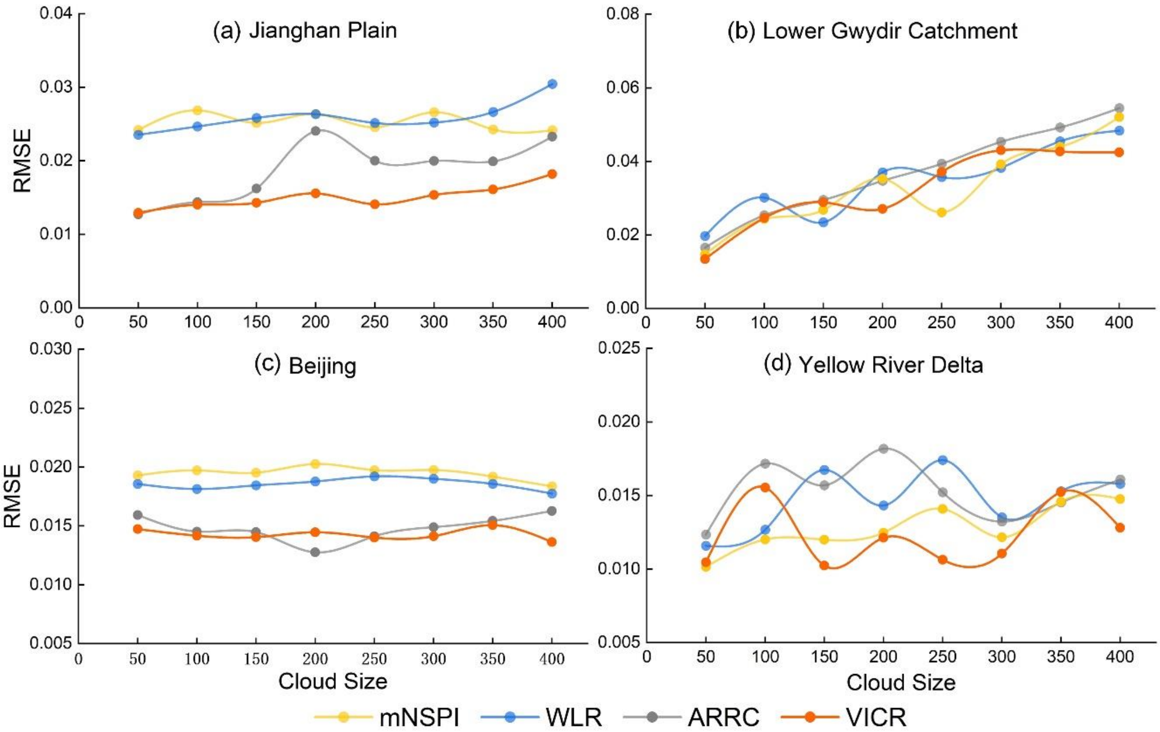

Fig. S6. The RMSEs of the reconstructed images from mNSPI, WLR, ARRC, and VICR at **red** band for cloud sizes ranging from 50×50 pixels to 400×400 pixels. Note that the RMSEs were calculated for the 50×50 pixels in the center of the clouds.

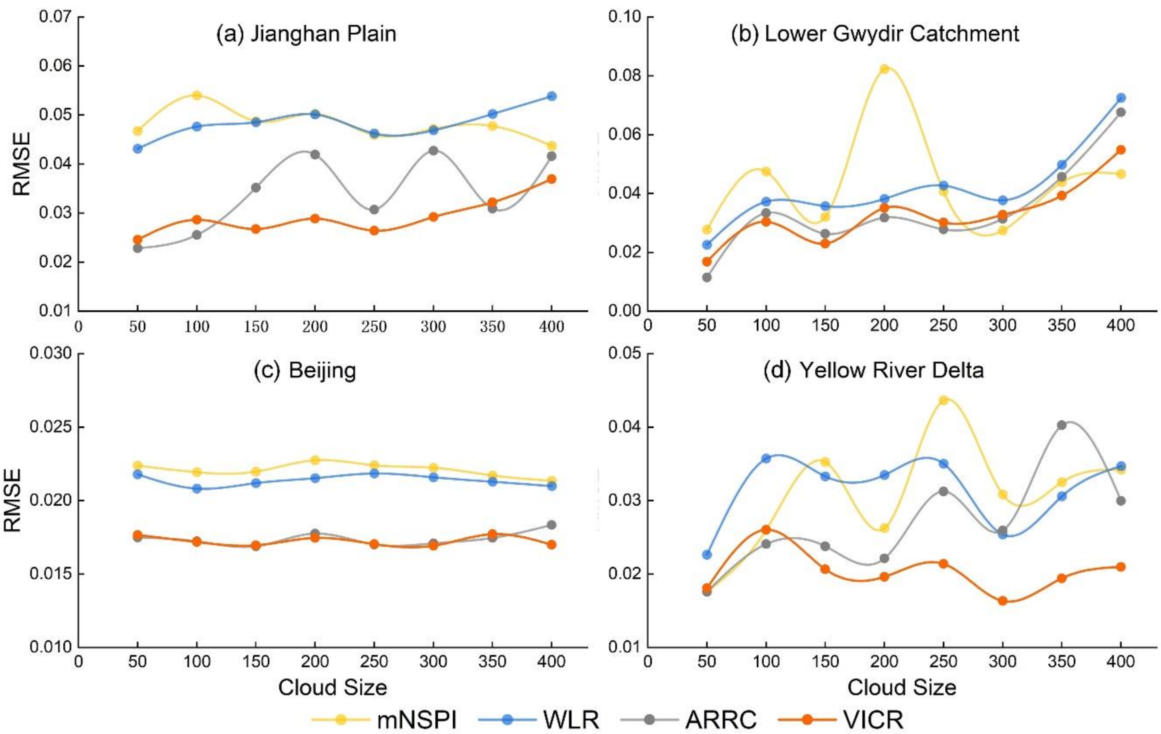

Fig. S7. The RMSEs of the reconstructed images from mNSPI, WLR, ARRC, and VICR at **SWIR1** band for cloud sizes ranging from 50×50 pixels to 400×400 pixels. Note that the RMSEs were calculated for the 50×50 pixels in the center of the clouds.

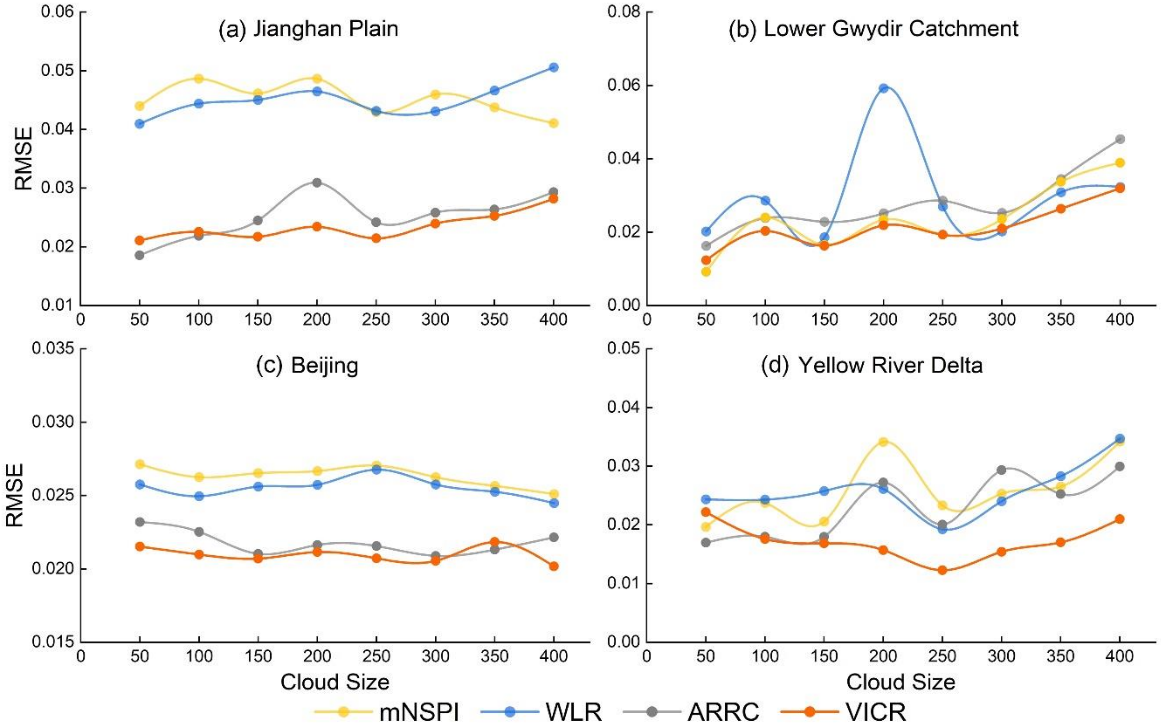

Fig. S8. The RMSEs of the reconstructed images from mNSPI, WLR, ARRC, and VICR at **SWIR2** band for cloud sizes ranging from 50×50 pixels to 400×400 pixels. Note that the RMSEs were calculated for the 50×50 pixels in the center of the clouds.

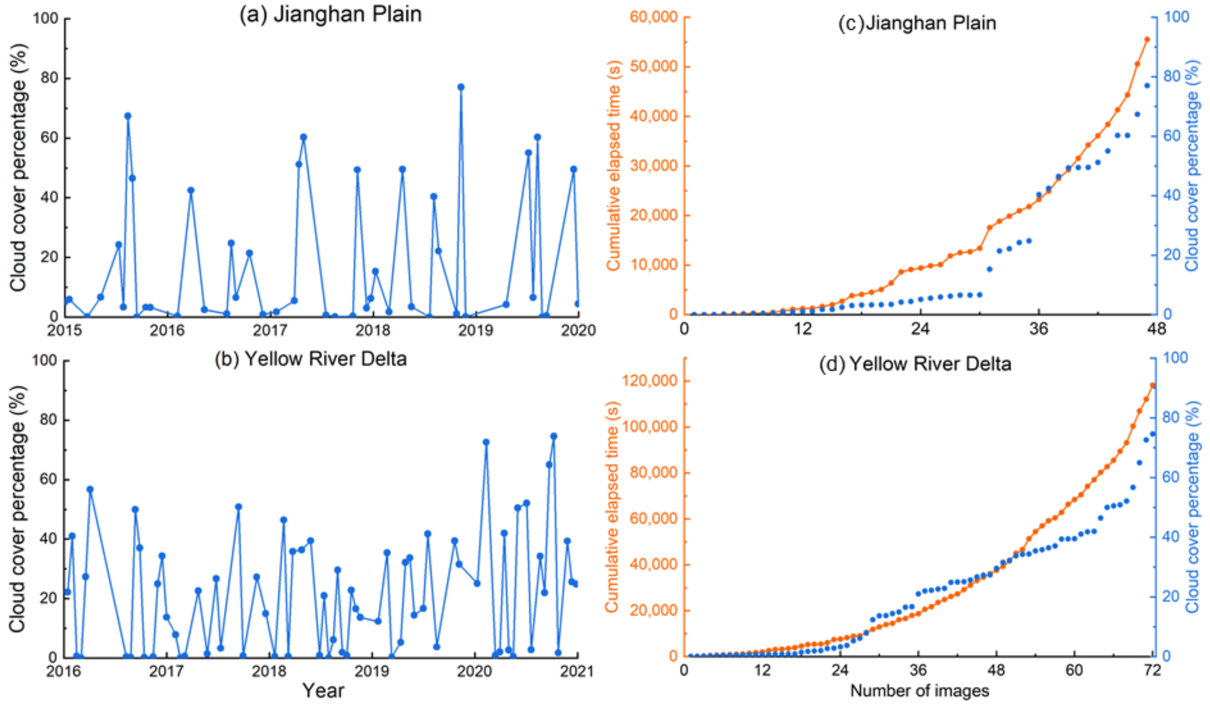

Fig. S9. Cloud cover percentage in the time-series Landsat images in (a) Jianghan Plain and (b) Yellow River Delta in Experiment VI. VICR was applied to the images in order of cloud cover rate, and the cumulative elapsed time in seconds are illustrated in (c) for Jianghan Plain and (d) for Yellow River Delta.

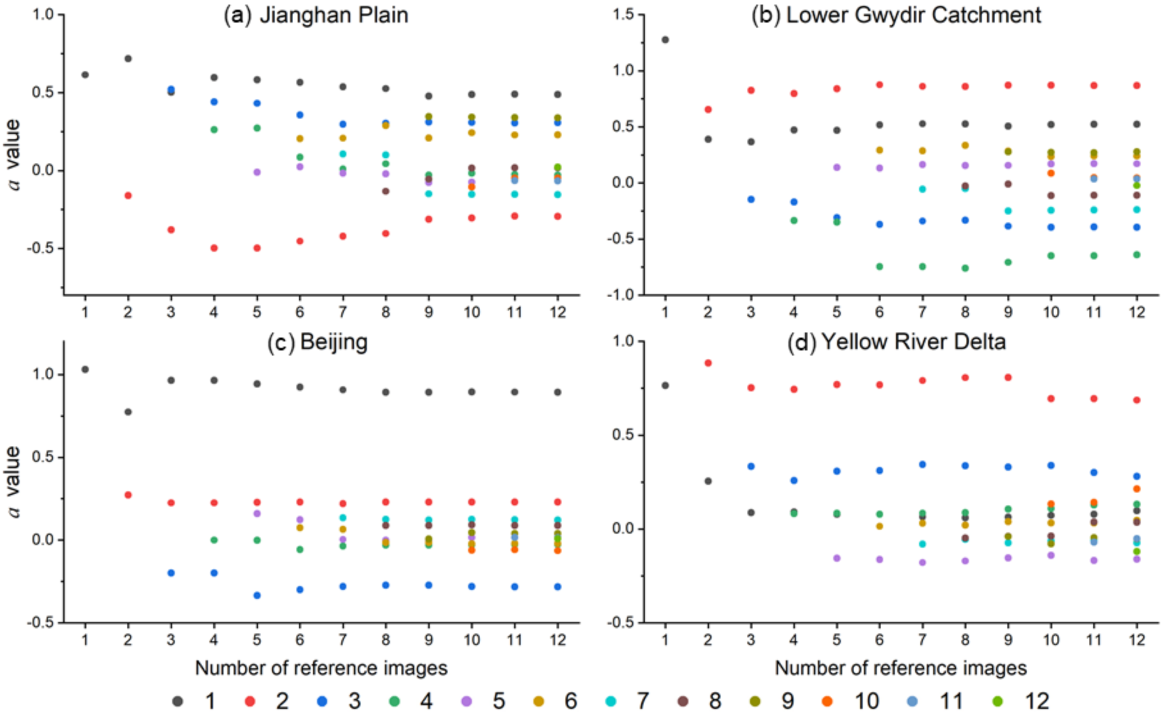

Fig. S10. The values of coefficient a_t in NIR band when 1~12 reference images were used for (a) Jianghan Plain, (b) Lower Gwydir Catchment, (c) Beijing and (d) Yellow River Delta.

(A) Jianghan Plain

(B) Lower Gwydir Catchment

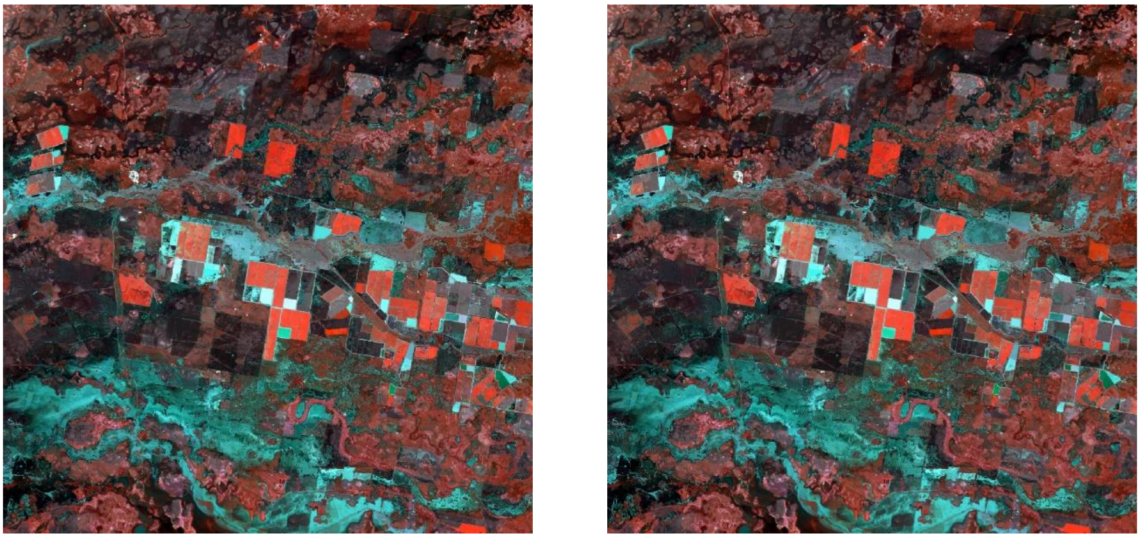

(C) Beijing

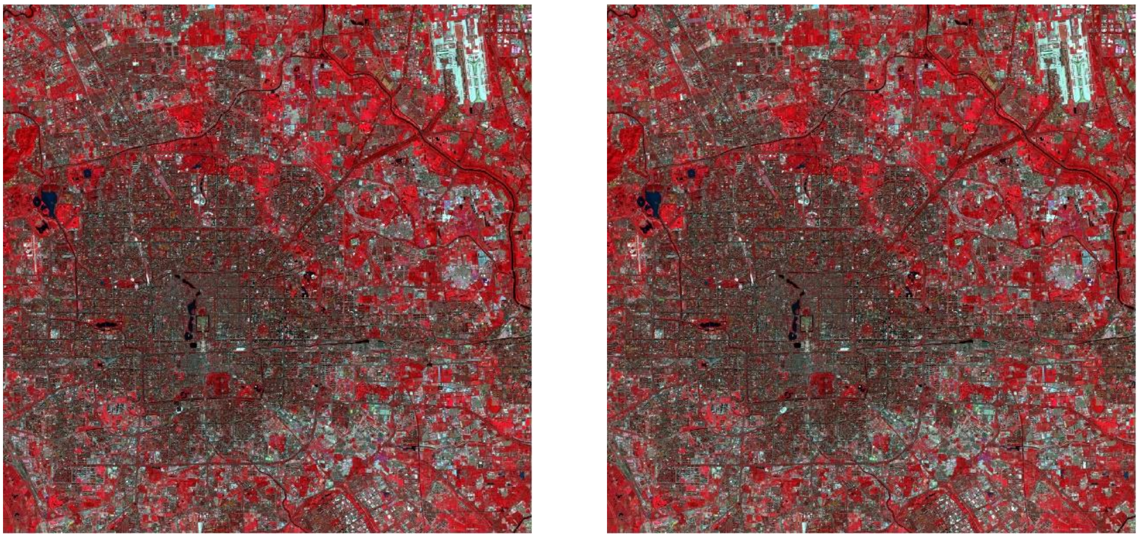

(D) Yellow River Delta

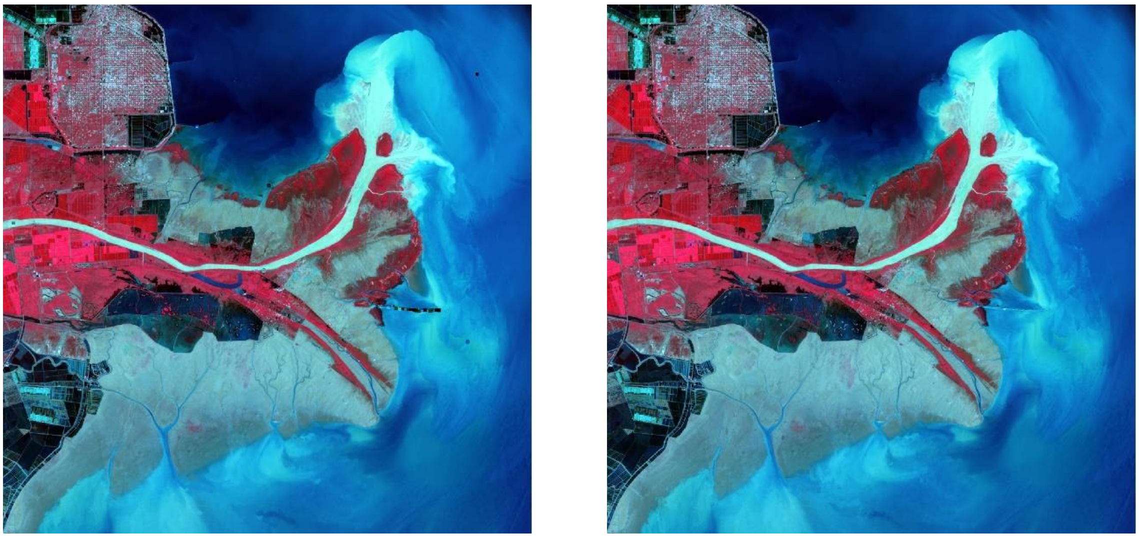

Fig. S11. Left column: cloud removed image following the same procedure in Experiment III; Right column: cloud removed image following the time-series image cloud removal procedure in Experiment VI.

Table S1. Input Landsat images for time-series cloud removal procedure in Section 5.4 for Jianghan Plain, Lower Gwydir Catchment, Beijing and Yellow River Delta.

Jianghan Plain		Lower Gwydir Catchment		Beijing		Yellow River Delta	
Image date	Cloud cover percentage	Image date	Cloud cover percentage	Image date	Cloud cover percentage	Image date	Cloud cover percentage
07/09/14	22.8%	05/18/04	0.0%	09/25/16	46.1%	09/14/17	50.9%
10/13/14	17.0%	06/03/04	0.0%	10/11/16	0.5%	09/30/17	0.8%
11/14/14	0.0%	06/19/04	0.3%	11/12/16	43.6%	11/17/17	27.2%
12/16/14	1.0%	07/05/04	0.0%	11/28/16	0.2%	12/19/17	14.9%
01/01/15	5.1%	07/21/04	25.1%	12/14/16	0.1%	01/20/18	0.6%
01/17/15	5.9%	08/06/04	0.0%	01/31/17	0.0%	02/21/18	46.5%
03/22/15	0.1%	08/22/04	0.0%	03/04/17	0.1%	03/09/18	0.6%
05/09/15	6.6%	09/23/04	0.0%	04/05/17	35.1%	03/25/18	35.8%
07/12/15	24.2%	10/09/04	0.0%	04/21/17	0.5%	04/26/18	36.4%
07/28/15	3.3%	10/25/04	0.0%	05/07/17	0.1%	05/28/18	39.5%
08/13/15	67.4%	11/10/04	50.0%	05/23/17	0.1%	06/29/18	0.8%
08/29/15	46.5%	11/26/04	0.0%	07/10/17	0.0%	07/15/18	21.0%
09/14/15	**0.0% (49.4%)**	**12/12/04**	**0.0% (71.3%)**	**09/12/17**	**0.1% (35.1%)**	**07/31/18**	**0.1% (41.8%)**
10/16/15	3.3%	12/28/04	0.0%	09/28/17	0.1%	08/16/18	6.2%
11/01/15	3.2%	01/13/05	0.0%	10/30/17	0.2%	09/01/18	29.6%
02/05/16	0.4%	01/29/05	0.0%	11/15/17	0.1%	09/17/18	1.9%
03/24/16	42.5%	02/14/05	0.0%	12/01/17	0.2%	10/03/18	0.8%
05/11/16	2.5%	03/02/05	0.0%	12/17/17	0.2%	10/19/18	22.8%
07/30/16	1.1%	03/18/05	71.3%	01/02/18	6.9%	11/04/18	16.5%
08/15/16	24.8%	04/03/05	0.0%	02/03/18	0.0%	11/20/18	13.7%
08/31/16	6.6%	04/19/05	0.0%	04/08/18	0.0%	01/23/19	12.3%
10/18/16	21.4%	05/05/05	0.0%	06/27/18	0.9%	02/24/19	35.4%
12/05/16	0.9%	05/21/05	0.0%	07/29/18	62.6%	03/12/19	0.3%
01/22/17	1.7%	06/06/05	0.1%	10/01/18	0.1%	04/13/19	5.3%
03/27/17	5.5%	07/24/05	0.0%	10/17/18	0.1%	04/29/19	32.2%

Image in bold font represents the target image. It is cloud free and we simulated cloud cover using real cloud shapes in Fig. 12. The simulated cloud coverages are in the parentheses.